

FLOW AND TEXTURE MODELING OF LIQUID CRYSTALLINE MATERIALS

Alejandro D. Rey

Department of Chemical Engineering, McGill University,
3610 University Street, Montreal, QC, Canada H3A 2B2

E-mail: alejandro.rey@mcgill.ca

ABSTRACT

A review of flow and texture modeling of liquid crystalline materials with emphasis on carbonaceous mesophases is presented. Two models of nematodynamics are presented and discussed in terms of their ability to resolve time and length scales likely to arise in typical rheological and processing flows. Defect physics and rheophysics are integrated with nematodynamics and specific mechanisms of defect nucleation and annihilation are used to derive texture scale power laws. The integrated nematodynamics models specialized to carbonaceous mesophases are used to analyze: (i) linear and nonlinear viscoelasticity, (ii) rheological flows, and (iii) carbon fiber and flow-induced textures. The linear and nonlinear viscoelasticity reveals the essential nature of these materials : coupling between flow-induced orientation and orientation-induced flow, elastic storage through orientation gradients, and anisotropy. The rheological flow simulations, shown to be in excellent agreement with experimental data, reveal several liquid crystal specific rheological characteristics including shear thinning due to anisotropic viscosities and flow-induced orientation, and negative first normal stress difference due to orientation nonlinearities in the shear stress. Nematodynamic predictions are shown to follow a Carreau-Yasuda liquid crystal equation. Nematodynamics predictions rationalize shear-induced texture refinement in terms of defect nucleation and coarsening mechanisms and are used to derive texture scaling relations in terms of macroscopic, molecular, and flow time scales. This knowledge is then condensed into a generic texture-flow diagram that specifies the required temperature and Deborah number required to produce well oriented monodomain materials. The fine details of mesophase structuring by flow through screens are shown to be captured by nematostatic simulations. Finally the mechanisms behind the carbon fiber textures produced by melt spinning of carbonaceous mesophases are elucidated. The proven range and predictive accuracy of nematodynamics to simulate flows of textured mesophases and the ever-growing industrial interest in lower cost high performance super-fibers and functional materials will fuel the evolution of liquid crystal rheology and processing science for years to come.

KEYWORDS: Rheology of carbonaceous mesophases; Discotic liquid crystals; Defect rheo-physics; Flow structuring; Carbon fiber structures

1. INTRODUCTION

Liquid crystals are synthetic and biological anisotropic viscoelastic textured materials [1-7]. They are used as precursor materials in the manufacturing of fibers, films, foams, moldings, blends and composites [2,6,7]. Liquid crystals are also used as functional materials in a variety of applications including sensors, electro-optical devices, lubricants, separations, actuators, and reactive media [2,3]. Figure 1 shows a flow chart that summarizes the dual role of LCs as structural and functional materials in technological applications. In some instances, such as carbon fibers spun from carbonaceous mesophases [6], the mechanical and heat transfer properties are optimized, combining the advanced mechanical properties with the functionality of enhanced heat conduction. Sensor applications include thermal, pressure, and chemical sensors based on different interactions of the liquid crystal molecular organization with propagating light [3]. For example, small molar mass LCs are used as biosensor to detect the presence of proteins, viruses and biomacromolecules; the device is based on “liquid crystal vision”, based on the fact that insertion of particles or macromolecular assemblies into LCs leads to distortions in the molecular organization which are easily detectable with light transmission [8,9]. Electro-optical devices are a major application of low molar mass LCs due to their ability to respond to applied electric fields and their fast response time; since the optic axis of the material is changed by the external field, light transmission between cross polars can be modulated [1]. Other functionalities such as lubrication depend on their unique anisotropic viscoelastic nature, where the orientation-dependence of the viscosity is manipulated by bounding surfaces [10]. Liquid crystal polymers and oligomers are processed into high performance fibers essentially using conventional polymer processing operations, such as injection molding, fiber spinning, and blow-molding

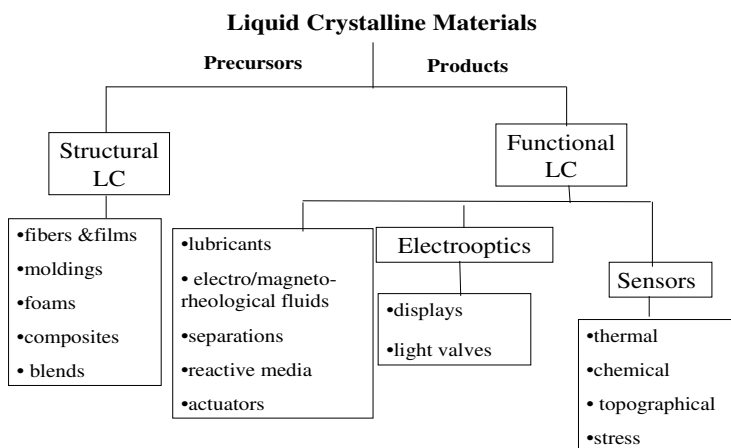


Figure 1. Flow chart of technological applications of liquid crystalline materials as structural and functional materials.

[2,6,11]. Flow-processes and rheology play a significant role in the processing of LC precursors into high performance materials, including flow-induced orientation, viscoelastic relaxation, anisotropic viscoelasticity, and flow-induced textural transformations [12,13]. The role of rheology in the performance of functional LC devices include orientation-induced flow, viscosity reduction, and flow-induced structural changes. For example in electro-optical devices reduction of the rotational viscosity by blending is a widely used device strategy [1]. The role of flow and viscosity for electro-optical devices is summarized in textbooks [1,3]. This review focuses on rheological applications relevant to structural LC materials.

Figure 2 presents a more detailed description of the different LC precursors used for structural applications of interest in this review. The left stream of the chart corresponds to synthetic LCs, and includes lyotropic LCPs (solution-based) such as Kevlar, thermotropic LCs (temperature-based) including thermotropic LCPs such as Vectra, and carbonaceous mesophases [2,14]. The middle stream corresponds to various LC blends, such as in-situ polymer composites (thermoplastic matrix and TLCP fibers) and mesophase carbon matrix -carbon fiber composites [2,14].

The right stream corresponds to biological LCs and includes spider silk and plywood biological composites [15-22]. Since the rheology of nematic LCPs is abundant and includes many extensive reviews and textbooks, here we focus on novel carbonaceous mesophases (CMs), which form the basis for high performance carbon fibers, carbon foams, carbon-carbon composites and nanocomposites [6,11]. The interest in CM as a precursor material is the ability to display liquid crystallinity, where the orientational order is responsive to external flow fields, electromagnetic fields, and confinement effects [23,24].

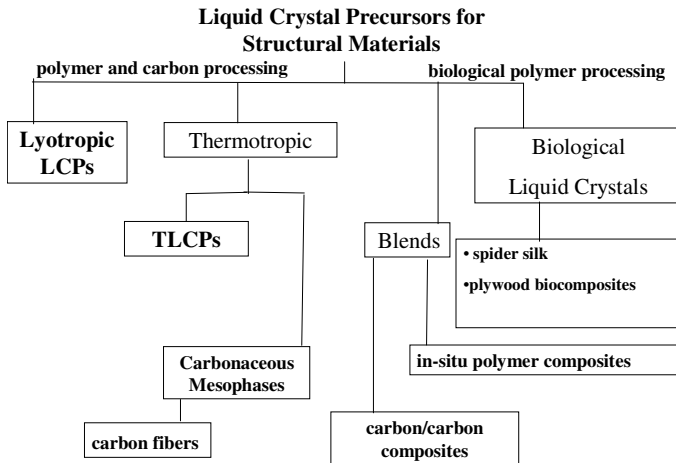


Figure 2. Flow chart of representative liquid crystalline materials used as precursors for structural materials

Following the approach established by White and co-workers [23,25], it proves useful to view flow-processing of these liquid crystalline precursors as a microstructural reactor, where orientation, domains, defects, and textures are manipulated by shear and extension deformation rates and where the flow patterns, secondary flows, and hydrodynamic interactions are tightly coupled to liquid crystalline order. This LC flow-analysis paradigm shown in Figure 3 is a close loop that couples the velocity and microstructure through flow-induced orientation and its converse, orientation induced flow and with both processes feeding into defect and textures. While flow-induced orientation is well-known and characterized in flexible and rigid rod polymers, the full range of effects arising from orientation-induced flow, such as back-flow, transverse flow, and hydrodynamic interactions during defect-defect annihilation, is less characterized. Furthermore flow-induced textural transformations can only be understood using defect physics and rheophysics. The closed loop shown in Figure 3 can be achieved at a macroscopic level using a vector orientation description (Leslie-Ericksen model [1]) or at the mesoscopic level (Landau-de Gennes model [12,26-31]) using the second moment of the orientation distribution function of the liquid crystals. Only the latter captures important features such as singular defect nucleation, singular defect-defect reactions, and singular defect-flow interactions; the difference between singular and non-singular defects is explained below.

Carbonaceous mesophases containing large polynuclear aromatic hydrocarbon molecules are discotic nematic LCs obtained from petroleum pitches and synthetic naphthalene precursors. The flat-like polyaromatic molecules are well-approximated by a uniaxial disk-like geometry, with an approximate average molecular weight of 2000 [32-36]. As in other nematic LC phases [1], carbonaceous mesophases are anisotropic, viscoelastic, and textured materials, possessing orientational order; the orientational order is captured by the average orientation or director \mathbf{n} , where $\mathbf{n} \cdot \mathbf{n} = 1, \mathbf{n} = -\mathbf{n}$; the latter indicates that the phase is apolar. The polymorphism of disk-like LCs includes the nematic and columnar phases, as shown in Figure 4 [1].

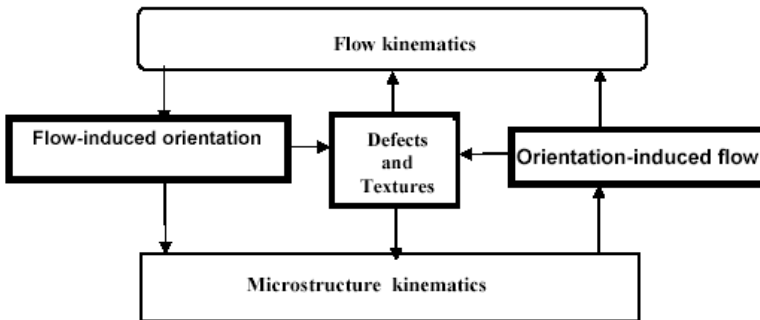


Figure 3. Schematic of velocity-microstructure kinematics-defect and texture couplings that build the nematodynamic cycle.

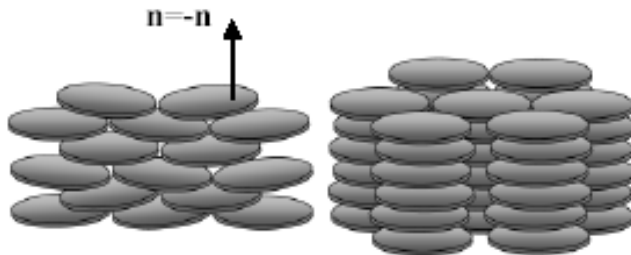


Figure 4. Nematic and columnar phases of disk-like mesogens; \mathbf{n} is the director.

The nematic state has orientational order given by the director \mathbf{n} while the columnar phase has orientational and 2D positional order. For carbonaceous mesophases no substantial reports of the columnar phase appear to have been made.

The main process used to produce spinnable CMs are: (a) the liquid phase pyrolysis of coal tar or petroleum pitches, (b) catalytic polymerization of pure aromatic hydrocarbons, such as naphthalene [37-39], and (c) supercritical solvent extraction of mesophase fractions from isotropic pitches [40]. Figure 5 shows a schematic of the material transformations brought about during the pyrolysis of isotropic pitches. When the temperature is greater than 350°C, optically anisotropic spherulites, emerge in the isotropic matrix [41-43] due to polymerization reactions continue the poly-aromatic molecules become larger and the anisotropic phase grow

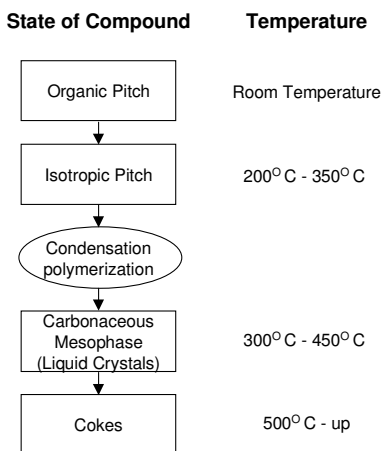


Figure 5. Changes in the non-volatile organic compounds like coal or petroleum pitches brought about by heating in the absence of air. Adapted from Ref. [45].

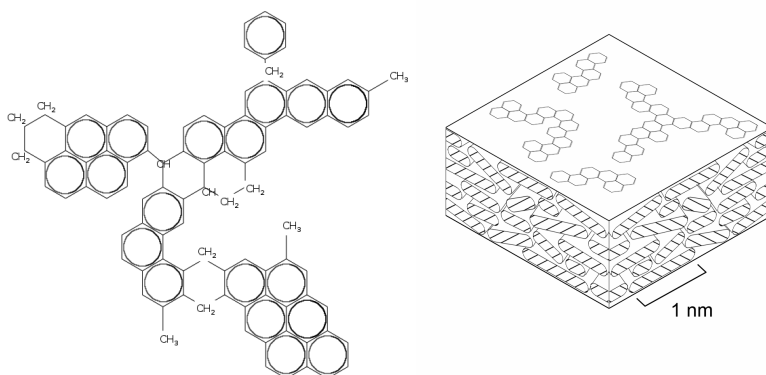


Figure 6. Typical molecule of a heat soaked mesophase pitch (Adapted from Ref. [47]) and molecular organization (Adapted from Ref. [23])

and becomes more viscous. The process is similar to polymerization-induced phase separation observed in polymeric materials. When the molecules reach an average molecular weight of approximately 2000, they are apparently, sufficiently large and flat to favor the formation of a liquid crystalline discotic nematic phase.

The spherulites that form during the formation of the mesophase are easily observed due their optical anisotropy. Attractive forces among the spherules give rise to droplet coalescence and overall growth of the mesophase. The structure of the spherules and the molecular organization of the disc-like poly-aromatic molecules within the spherulites have been described in [44]. A typical molecule of a heat-soaked mesophase pitch and molecular organization are illustrated in Figure 6.

Conventional high-speed melt spinning process is employed to convert palletized mesophase pitch into carbon fibers [46]. The extruder melts and pressurizes the pitch, and pumps it through the spin pack. The molten pitch is filtered before being extruded through the multi-holed spinneret. The pitch is subjected to high extensional and shear stresses as it approaches and flows through the spinneret capillaries. The associated flow-induced torques tend to align the liquid crystalline pitch in a plane normal to the extension plane. The average orientation of the disc-like molecules on the cross-sectional plane depends on the processing conditions, the flow geometry, and the material properties of the pitch, and has significant impact on the final properties of the mesophase carbon fibers. Upon emerging from the spinneret capillaries, the mesophase fibers are drawn to improve the axial orientation, and are collected on a windup device.

Mesophase carbon fibers exhibit a spectrum of transverse textures that are associated with various thermo-mechanical properties. The microstructural features of the textures are defined by the spatial arrangement of the constituting flat disc-like polyaromatic molecules in the fibers of different cross sectional shapes. Some most typical examples, reported in the literature [48] are shown in Figure 7. The lines

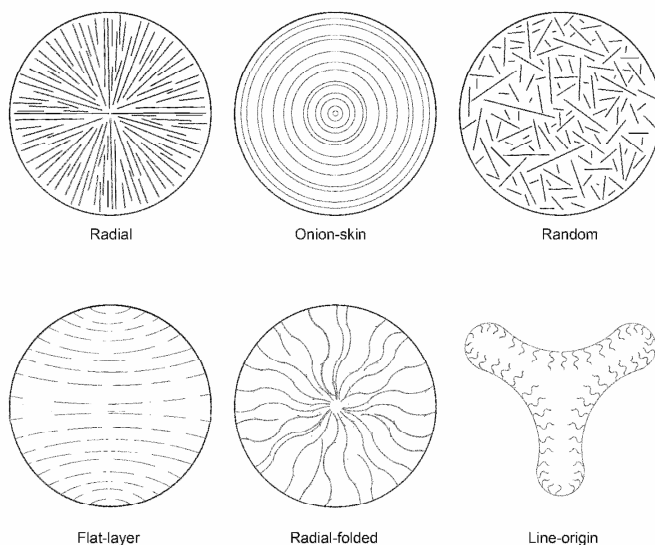


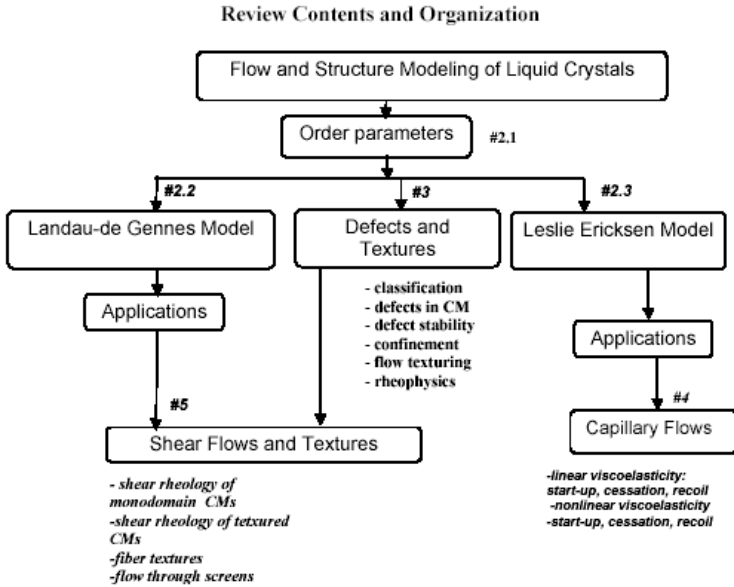
Figure 7. Schematics of the observed mesophase carbon fiber textures. The lines represent the locus of the side view of the disc-like molecules, such that in a radial texture, the discs orient with their unit normals describing circles concentric with the fiber axis, while in an onion-like texture, the discotic molecules themselves follow a circular paths concentric with the fiber axis. Adapted from Ref. [6,48].

represent loci of the side view of the disk like molecules. In a radial texture, the discotic molecules orient with their unit normals describing circles concentric with the fiber axis, while in an onion-like texture, the discotic molecules themselves follow a circular paths concentric with the fiber axis. In addition to this, the fiber cores may be isotropic or anisotropic, the latter would give rise to singular lines running along the fiber core. Although the stiffness and thermal conductivity of mesophase carbon fibers are generally high, however, these properties can vary significantly with fiber textures [49-51]. Different routes are taken to control the fiber cross-section molecular architecture including the pretreatment of mesophase pitches, the constitution and spinnability of pitches, the spinning conditions, the spinneret geometry, the processing conditions, the fiber size and shape, flow through screens and filters, and numerous other factors (see for example [6,48]).

The objectives of this review are: (i) to present the most widely used models for liquid crystal flows (nematodynamics) (ii) to adapt the nematodynamics models to carbonaceous mesophases by taking into account their intrinsic molecular anisotropy, (iii) to present a comprehensive discussion of defect and textures physics, (iv) to present predictions and validations of rheological and processing flows, and (v) to

present experimentally-validated predictions process-induced texturing including carbon fibers architectures and texturing by flow through screens.

The organization of this review is presented in the flow chart below.



Section 2 presents the order parameters for the nematic phase, the relevant length and time scales and the Leslie-Ericksen vector model [1] and the Landau de Gennes quadrupolar order parameter model [31]. Section 3 presents a classification of defects and textures, defects in CMs, defect stability, effects of confinement, defect nucleation processes, the rheophysics of defects, and scaling laws for texture refinement under shear. Section 4 presents representative applications of the Leslie-Ericksen model to the linear and nonlinear viscoelasticity of CMs under pressure driven capillary flows, including start-up and cessation of flow; these results best highlight the coupled nature of flow-induced orientation and orientation-induced flow in nematodynamics. Section 5 presents representative applications of the LdG model to the shear flow of CMs and texture processes. Steady and transient responses are validated with experimental results. The LdG viscosity prediction is cast into a Carreau-Yasuda model and together with the texture scaling laws, expressions of viscosity as a function of texture scale are derived. A texture diagram that indicates the relation between temperature and the Deborah number required for attaining well-aligned monodomains is given. Predictions of carbon fiber textures and texturing by flow-through screens are validated with experiments. Finally, section 6 summarizes the results, present conclusions on the utility of these modeling tools to better characterize and process LC materials, and ends with future challenges.

2. THEORIES AND RHEOLOGICAL MODELS

2.1. Order Parameters, Length Scales and Time Scales

The usual description of orientational order in nematic liquid crystal is based on the normalized orientation distribution function $ODF(\mathbf{u})$, where \mathbf{u} is the orientation of the disk normal, given by [52]:

$$ODF(\mathbf{u}) = \frac{1}{2\pi} f_o + \frac{3 \times 5}{2\pi \times 2} Q^2_{ij} f^2_{ij} + \frac{3 \times 5 \times 7 \times 9}{2\pi \times 2 \times 3 \times 4} Q^4_{ij} f^4_{ij} + \dots \quad (1)$$

where $f_o, f^2_{ij}, f^4_{ijkl}, \dots$ are orthogonal surface spherical harmonics and where the coefficients of the Fourier expansion, Q^2, Q^4, \dots are symmetric and traceless tensors found using orthogonality. The quadrupolar tensor order parameter Q^2 used in the Landau-de Gennes viscoelastic model is [1] :

$$\mathbf{Q} \equiv Q^2 = \int_{\delta^2} f(\mathbf{u}) \mathbf{f}^2 dA = \int_{\delta^2} f(\mathbf{u}) \left(\mathbf{u}\mathbf{u} - \frac{\delta}{3} \right) dA = \left\langle \mathbf{u}\mathbf{u} - \frac{\delta}{3} \right\rangle \quad (2)$$

where δ^2 is half the unit sphere. Expanding \mathbf{Q} in terms of eigenvectors we find :

$$\mathbf{Q} = \mu_n \mathbf{nn} + \mu_m \mathbf{mm} + \mu_l \mathbf{ll}; \mathbf{n} \cdot \mathbf{m} = \mathbf{n} \cdot \mathbf{l} = 0; \mu_n + \mu_m + \mu_l = 0 \quad (3)$$

The three nematic states are : (i) isotropic : $\mu_n = \mu_m = \mu_l = 0$; (ii) uniaxial : $\mu_n \neq \mu_m = \mu_l$; (c) biaxial : $\mu_n \neq \mu_m \neq \mu_l$. Another useful expression for \mathbf{Q} in terms of the scalar order parameters (S,P) is :

$$\mathbf{Q} = S \left(\mathbf{nn} - \frac{\delta}{3} \right) + \frac{P}{3} (\mathbf{mm} - \mathbf{ll}) \quad (4)$$

For uniaxial phases \mathbf{Q} is given in terms of a temperature-dependent scalar order parameter $S(T)$ and the average molecular orientation or director \mathbf{n} : $\mathbf{Q} = S(\mathbf{nn} - \mathbf{I}/3)$. A useful visualization of $\mathbf{Q} + \mathbf{I}/3$, are parallelepipeds shown in Figure 8.

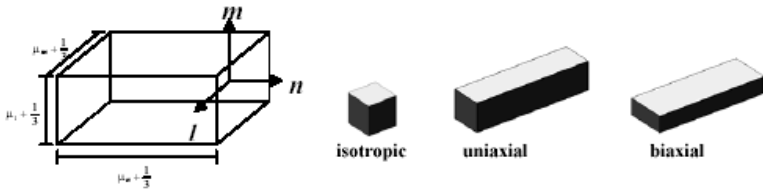


Figure 8. Representation of the tensor $\mathbf{Q} + \mathbf{I}/3$ (left), and cuboids for the isotropic, uniaxial and biaxial phases.

In this review we consider two models: (1) the Leslie-Ericksen **n**-vector model for uniaxial nematics, and (2) the Landau-de Gennes **Q**-tensor model for nematic and cholesteric LCs. The former is used to describe nematodynamics in the absence of singular defects at low Deborah (D_e) numbers, while the latter is used to describe nematodynamics of textured materials at arbitrary D_e numbers. The description of defect singularities with the LE is possible using analytical techniques and domains that exclude defect cores (i.e. introducing a cut-off) and hence not useful in the presence of many mobile defects; the LE model can only describe non-singular defects such as continuous orientation walls. In the LdG tensor model the singularity is not present because the scalar order parameters are continuous in the core. Figure 9 shows a $\frac{1}{2}$ disclination line in a singular **n**-vector description and in the smooth **Q**-tensor model. Note that the cuboid representation shows the characteristic biaxial core region.

The LdG has an external length scale ℓ_e and an internal length scale ℓ_i as follows [12,26]:

$$\ell_e = H, \quad \ell_i = \sqrt{\frac{L}{3ckT^*}}, \quad \square = \left(\frac{\ell_e}{\ell_i}\right)^2 = \frac{3ckT^*}{L/H^2} \gg 1 \quad (5)$$

where H is the system size, L (energy/length) is a characteristic orientation elasticity constant associated with gradients in the directors (**n,m,l**) and ckT^* is the energy per unit volume associated with molecular elasticity (S,P) ; c is the concentration per unit volume, k is the Boltzmann constant, and T^* is the isotropic-nematic transition temperature. The external scale is associated with micron-scale changes in (**n,m,l**) and the internal length scale ℓ_i is associated with nano-scale changes in (S,P), as in the disclination core shown in Figure 9. The ratio of molecular ordering energy to orientation elasticity R, or ratio of length scales square, is of the order of 10^6 - 10^9 . In the LE model R is assumed to be infinity and hence the scalar order parameters (S,P) are not taken into account. The external τ_e and internal τ_i time scales of the LdG model are ordered as follows [53,54]:

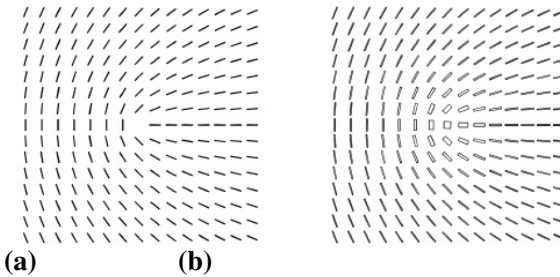


Figure 9. (a) Director **n** singular description and (b) **Q**-tensor smooth description of a $\frac{1}{2}$ edge disclination. The LdG is able of resolving the biaxial core of the disclination.

$$\tau_e = \frac{\eta H^2}{3L}, \quad \tau_i = \frac{1}{D_r}, \quad \tau_e \gg \tau_i \quad (6)$$

where D_r is the bare rotational diffusivity and $\eta = ckT^*/D_r$. The external time scale describes slow orientation variations and the internal length scale describes fast order parameter variations. In the LE model $\tau_i=0$ and no molecular dynamics are taken into account. Finally the presence of shear flow of rate $\dot{\gamma}$ introduces a flow time scale τ_f and a flow length scale ℓ_f :

$$\tau_f = \frac{1}{\dot{\gamma}}, \quad \ell_f = \sqrt{\frac{D_{\text{orient}}}{\dot{\gamma}}}, \quad D_{\text{orient}} = \frac{LH^2}{3\tau_e} = \frac{L}{\eta} \quad (7)$$

where D_{orient} is the characteristic orientation diffusivity (length²/time). Related to the values of Deborah numbers we have two processes: (a) Orientation process ($D_e \ll 1$): the time scale ordering is $\tau_i < \tau_f < \tau_e$, the orientation processes dominate the rheology, and the scalar order parameter is close to its equilibrium value. In this regime the flow affects the eigenvectors of \mathbf{Q} , but does not affect the eigenvalues of \mathbf{Q} . Since LC are anisotropic, shear thinning, non-monotonic stress growth and first normal stress differences are possible (b) Molecular process ($D_e > 1$): the time scales ordering is $\tau_f < \tau_i < \tau_e$, and the flow affects the eigenvectors and eigenvalues of \mathbf{Q} . The dimensionless Ericksen number E_r and Deborah number [26] are given by:

$$E_r = \left(\frac{\ell_e}{\ell_f}\right)^2 = \frac{3\tau_e}{\tau_f} = \frac{\dot{\gamma}H^2\eta}{L} \quad D_e = \frac{E_r}{R} = \left(\frac{\ell_i}{\ell_f}\right)^2 = \frac{\tau_i}{6\tau_f} = \frac{\dot{\gamma}}{6D_f} \quad (8)$$

To characterize the degree of ordering in the LC phase a dimensionless temperature $U=3T^*/T$ is used. Hence the most general parametric space for LdG nematodynamics is span by $(1/U, \square, E_r)$ while for the LE nematodynamics it is E_r .

2.2. Leslie Ericksen Nematodynamics

2.2.1. *Bulk and Interfacial Equations*

The LE equations consist of the linear momentum balance and director torque balance with additional constitutive equations for stress tensor \mathbf{T} , elastic torque $\mathbf{\Gamma}^e$ and viscous torque $\mathbf{\Gamma}^v$ [1,13,55]. The mass and linear momentum balance equations are:

$$\nabla \cdot \mathbf{v} = 0, \quad \rho \dot{\mathbf{v}} = \mathbf{f} + \nabla \cdot \mathbf{T} \quad (9)$$

where \mathbf{f} is the body force per unit volume, \mathbf{v} is the linear velocity, and a superposed dot represents the material time derivative of the velocity. The constitutive equation for the total stress tensor \mathbf{T} is given by:

$$\mathbf{T} = -p\mathbf{I} - \frac{\partial f_g}{(\partial \nabla \mathbf{n})^T} \cdot \nabla \mathbf{n} + \alpha_1(\mathbf{nn} : \mathbf{A})\mathbf{nn} + \alpha_2\mathbf{nN} + \alpha_3\mathbf{Nn} + \alpha_4\mathbf{A} + \alpha_5\mathbf{nn} \cdot \mathbf{A} + \alpha_6\mathbf{A} \cdot \mathbf{nn} \quad (10)$$

$$2\mathbf{A} = (\nabla \mathbf{v} + (\nabla \mathbf{v})^T), \quad \mathbf{N} = \dot{\mathbf{n}} - \mathbf{W} \cdot \mathbf{n}, \quad 2\mathbf{W} = (\nabla \mathbf{v} - (\nabla \mathbf{v})^T) \quad (11)$$

where p is the pressure, \mathbf{I} is the unit tensor; $\{\alpha_i, i = 1 \dots 6\}$ are the six Leslie viscosity coefficients; \mathbf{A} is symmetric rate of deformation tensor, \mathbf{N} is the Zaremba-Jaumann time derivative of the director, and \mathbf{W} is the vorticity tensor. The Frank elastic energy density f_g is given by:

$$2f_g = K_{11}(\nabla \cdot \mathbf{n})^2 + K_{22}(\mathbf{n} \cdot \nabla \times \mathbf{n})^2 + K_{33}(\mathbf{n} \times \nabla \times \mathbf{n})^2 \quad (12)$$

where $\{K_{ii}; ii = 11, 22, 33\}$ are the temperature-dependent three elastic constants for splay, twist, and bend, respectively, shown in Figure 10 for disks (top) and rods (bottom). Anisotropies and thermal dependence of the elastic constants are discussed in the literature [1,12,13].

The director torque balance equation is given by the sum of the viscous $\mathbf{\Gamma}^v$ and the elastic $\mathbf{\Gamma}^e$ torque:

$$\mathbf{\Gamma}^v + \mathbf{\Gamma}^e = 0 \quad (13)$$

$$\mathbf{\Gamma}^v = \mathbf{n} \times \mathbf{h}^v \equiv -\mathbf{n} \times (\gamma_1 \mathbf{N} + \gamma_2 \mathbf{A} \cdot \mathbf{n})$$

$$\mathbf{\Gamma}^e = \mathbf{n} \times \mathbf{h}^e \equiv -\mathbf{n} \times \left(\frac{\partial f_g}{\partial \mathbf{n}} - \nabla \cdot \frac{\partial f_g}{(\partial \nabla \mathbf{n})^T} \right)$$

where \mathbf{h}^v is the viscous molecular field, \mathbf{h}^e is the elastic molecular field, $\gamma_1 = \alpha_3 - \alpha_2$ is the rotational viscosity, and $\gamma_2 = \alpha_6 - \alpha_3 = \alpha_3 + \alpha_2$ is the irrotational torque coefficient. For thermotropic LCs, the rheological behavior is controlled by the temperature-

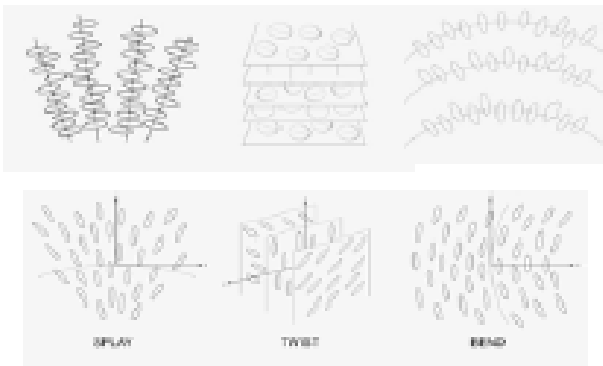


Figure 10. Schematics of the three gradient elasticity modes for disks (top) and rods (bottom): splay, twist, and bend.

dependent reactive parameter λ , given by:

$$\lambda = -\frac{\gamma_2}{\gamma_1} = -\frac{\alpha_2 + \alpha_3}{\alpha_3 - \alpha_2} \quad (14)$$

For disk-like (rod-like) nematics, two modes are possible: (a) $\lambda < -1$ ($\lambda > 1$) for the flow aligning mode in which nematics align close to the velocity gradient (velocity) direction and (b) $-1 < \lambda < 0$ ($0 < \lambda < 1$) for the non-aligning mode in which the director twists out of the shear plane at low shear rates.

The boundary conditions for the LE are obtained from the LE interfacial nematodynamics. The interfacial torque balance [10, 55-58] is the sum of the surface elastic torque Γ^{se} and the surface viscous torque Γ^{sv}

$$\Gamma^{\text{se}} + \Gamma^{\text{sv}} = \mathbf{0}; \Gamma^{\text{se}} = \mathbf{n} \times \mathbf{h}_e^s; \Gamma^{\text{sv}} = -\mathbf{n} \times \mathbf{h}_v^s \quad (15)$$

where \mathbf{h}_e^s is the surface elastic molecular field, and \mathbf{h}_v^s is the surface viscous molecular field. The elastic and viscous molecular fields (\mathbf{h}_e^s , \mathbf{h}_v^s) are three component vectors, with tangential ($\mathbf{h}_{e//}^s$, $\mathbf{h}_{v//}^s$) and normal ($\mathbf{h}_{e\perp}^s$, $\mathbf{h}_{v\perp}^s$) components with respect to the surface. The surface elastic molecular field \mathbf{h}_e^s is given by :

$$\mathbf{h}_e^s = -\frac{\partial f_s}{\partial \mathbf{n}} + \frac{\partial f_s}{\partial \nabla_s \mathbf{n}} - \mathbf{k} \cdot \frac{\partial f_g}{\partial \nabla \mathbf{n}} \quad (16)$$

where \mathbf{k} is the unit normal, ∇_s is the surface gradient operator, and f_s is the surface free energy density given by:

$$f_s = \gamma_0 + \gamma_{\text{an}} + \gamma_g, \quad \gamma_{\text{an}} = \gamma_2 (\mathbf{n} \cdot \mathbf{k})^2 + \gamma_4 (\mathbf{n} \cdot \mathbf{k})^4 \quad (17)$$

$$\gamma_g = \frac{1}{2} (\mathbf{K}_{22} + \mathbf{K}_{24}) \mathbf{k} \cdot \mathbf{g}, \quad \mathbf{g} = (\mathbf{n} \cdot \nabla_s) \mathbf{n} - \mathbf{n} (\nabla_s \cdot \mathbf{n}) \quad (18)$$

where γ_0 is the isotropic interfacial tension, and γ_{an} is the anisotropic contribution to the surface free energy, known as the anchoring energy, γ_g is the surface gradient contribution, and \mathbf{K}_{24} is the saddle-splay coefficient. For monomeric LCs the isotropic surface interfacial tension γ_0 is of the order of 10 ergs/cm², while the characteristic anchoring energy γ_{an} varies from 10⁻⁴-1 erg/cm² [59-61]. The director orientation that absolutely minimizes the surface free energy density is known as the easy axis of the

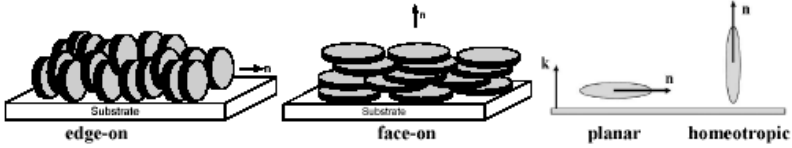


Figure 11. Schematics of the average orientation \mathbf{n} under strong anchoring conditions for CMs (edge-on and face-on) and for rod-like nematics (planar and homeotropic)

interface. For non-deforming interfaces the viscous surface molecular field takes into account dissipation due to orientational slip:

$$\mathbf{h}_v^s = \gamma_{1//}^s \mathbf{I}_s \cdot \frac{d\mathbf{n}}{dt} + \gamma_{1\perp}^s \mathbf{k}\mathbf{k} \cdot \frac{d\mathbf{n}}{dt} \quad (19)$$

where \mathbf{I}_s is the surface unit tensor, and $\gamma_{1//}^s$, $\gamma_{1\perp}^s$ are surface viscosities associated with tangential and normal rotations of the director. Two particular static director surface conditions are possible: (a) no torque condition, $\mathbf{k} \cdot \partial f_g / \partial \nabla \mathbf{n} = 0$, corresponding to the case of insignificant surface anchoring energy; (b) strong director surface anchoring, $\mathbf{n} = \mathbf{n}_{fix}$, corresponding to the case in which bulk gradient elasticity is insignificant with respect to surface anchoring energy. For CM two common types of fixed orientation are the face-on and edge-on states, and for rods they are known as planar and homeotropic, as shown in Figure 11.

2.2.2. Rheological Functions

The LE nematodynamics predicts the following rheological functions [1,13,62-64]:

(a) *Shear flow alignment*: at sufficiently large E_r , when $\lambda > 1$ (rods) or $\lambda < -1$ (discs) the stable shear flow-alignment angle θ_{al} is given by [1]:

$$2\theta_{al} = \cos^{-1} \left(\frac{1}{\lambda} \right) \quad (20)$$

where θ_{al} is the angle between \mathbf{n} and the velocity \mathbf{v} in the shear plane ($\mathbf{v} - \nabla \mathbf{v}$ plane).

(b) *Shear viscosities*: The three Miesowicz' shear viscosities (η_1 , η_2 , and η_3) that characterize viscous anisotropy are measured in a steady simple shear flow between parallel plates with fixed director orientations along three characteristic orthogonal directions: η_1 when the director is parallel to the velocity direction, η_2 when it is parallel to the velocity gradient, and η_3 when it is parallel to the vorticity axis, given by:

$$\eta_1 = (\alpha_3 + \alpha_4 + \alpha_6)/2, \quad \eta_2 = (-\alpha_2 + \alpha_4 + \alpha_5)/2, \quad \eta_3 = \alpha_4/2 \quad (21)$$

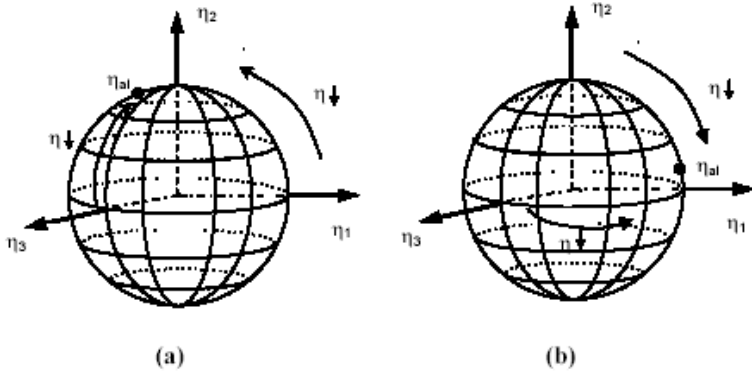


Figure 12. Orientation reduction mechanism predicted by the LE nematodynamics for disks (a) and rods (b). Adapted from Ref. [54].

For CMs (rods) it is found that $\eta_1 > \eta_3 > \eta_2$ ($\eta_1 < \eta_3 < \eta_2$) [12,54,65-69].

The shear viscosity under flow-alignment, defined by η_{al} is:

$$\eta_{al} = \frac{1}{2}(\eta_1 + \eta_2 - \gamma_1) + \frac{1}{4}\alpha_1 \left(1 - \left(\frac{1}{\lambda} \right)^2 \right) \quad (22)$$

and is slightly larger than η_2 for disks and η_1 for rods. Hence when $|\lambda| > 1$ as shear rate increases the LE nematodynamics describes an orientation viscosity reduction mechanism (OVR), as shown in Figure 12 [54]. For example, if one shears a CM sample with a random director orientation distribution the increasing effect of shear is to narrow the distribution with a peak that is aligned along the flow-alignment angle (close to the shear gradient direction) and hence the apparent viscosity will decrease with increasing shear since the flow-alignment angle is close to the minimum possible viscosity which for disks is η_2 .

Steady shear flow simulations indicate that for any arbitrary E_r , the LE nematodynamics can be fitted with the Carreau-Yasuda LC model [54]:

$$\eta_s = \frac{\eta - \eta_{al}}{\eta_0 - \eta_{al}} = \left[1 + (\tau E_r)^a \right]^{\frac{n-1}{a}} \quad (23)$$

where η_s is the scaled shear viscosity, n is the “power-law exponent”, a is a dimensionless parameter that describes the transition region between the zero-shear rate region and the power-law region, τ is a dimensionless time constant, η_0 is the zero shear rate viscosity. The first transition region in the Carreau-Yasuda liquid crystal model is defined by $E_r=1/a$, that is the Ericksen number at which flow

significantly affects the orientation. The second transition between the power law shear thinning regime and the flow-alignment regime is:

$$E_{\tau_{ST-FA}} = \frac{1}{\tau} \left(\frac{a}{c^{n-1}} - 1 \right)^{1/a} \quad (24)$$

where c is of the order of 10^{-3} .

(c) *Back-flow*: this process is the converse to orientation driven flow [1]. Except for pure homogeneous twist re-orientation, changes in the director orientation \mathbf{n} create flow. The re-orientation viscosities associated with splay, twist, and bend deformations (shown in Figure 10) are defined by [62,63]:

$$\eta_{\text{twist}} = \gamma_1, \quad \eta_{\text{splay}} = \gamma_1 - \alpha_3^2 / \eta_1, \quad \eta_{\text{bend}} = \gamma_1 - \alpha_2^2 / \eta_2 \quad (25)$$

These transient re-orientation viscosities are given by the rotational viscosity (γ_1) decreased by a factor introduced by the backflow effect. The general expression for the re-orientation viscosities can be re-written in a more revealing general form :

$$\eta_\alpha = \gamma_1 - (TC_i)^2 / \eta_i \quad (26)$$

where η_i denotes the corresponding Miesowicz' viscosity and TC_i the corresponding torque coefficient. Since twist is the only mode that creates no backflow [1] then $\eta_{\text{twist}} = \gamma_1$. For a bend distortion the backflow is normal to \mathbf{n} and hence the torque coefficient is α_2 , and the Miesowicz' viscosity is η_2 . On the other hand for a splay distortion the backflow is parallel to \mathbf{n} and hence the torque coefficient is α_3 , and the Miesowicz' viscosity is η_1 . The ordering in the re-orientation viscosities is: $\eta_{\text{twist}} > \eta_{\text{splay}}, \eta_{\text{twist}} > \eta_{\text{bend}}$.

(d) *Secondary flows*: whenever the director deviates from the shear plane a transverse flow will be generated since the viscosity tensor C_{ijkl} in the extra stress tensor (see eqn.(10)) is a function of the director [62,63]:

$$T_{ij}^{\text{extra}} = C_{ijkl} A_{lk} + D_{ijk} N_k \quad (27)$$

Hence under shear flow in the x-direction and 3D orientation $\mathbf{n}=(n_x, n_y, n_z)$ one must consider at a minimum a velocity of the form $\mathbf{v}=(v_x, 0, v_z)$.

(e) *First normal stress difference* N_1 : For nematic liquid crystals N_1 is a strong function of orientation and can have positive or negative values. Expressions for N_1 in terms of the director components n_x and n_y are [54]:

$$N_1 = t_{xx} - t_{yy} = \dot{\gamma} n_x n_y \left(\gamma_2 + \alpha_1 (n_y^2 - n_x^2) \right) \quad (28)$$

As the director circles the shear plane, the total number N_T of sign changes in N_1 is [54]:

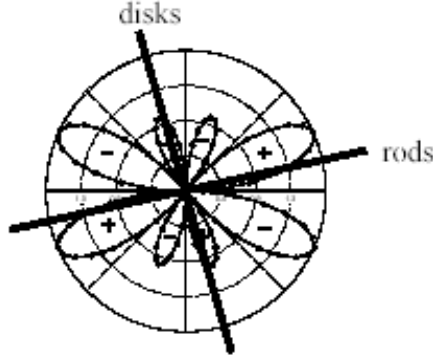


Figure 13. Sign and amplitude of the first normal stress difference N_1 as function as a function of the director polar angle from the flow direction. The lines indicate the flow-aligning angles of rods and disks. Adapted from Ref. [54].

$$N_T = N_{SC}(n_x) N_{SC}(n_y) N_{SC}\left(\left(\gamma_2 + \alpha_1(n_y^2 - n_x^2)\right)\right) \quad (29)$$

$$= 4N_{SC}\left(\left(\gamma_2 + \alpha_1(n_y^2 - n_x^2)\right)\right)$$

where N_{SC} denotes number of sign changes. The number of sign changes in n_x is 2, and similarly for n_y . We then find the two following material property-dependent outcomes:

$$|\gamma_2| < |\alpha_1| : N_T = 4 ; |\gamma_2| > |\alpha_1| : N_T = 4 \times 2 = 8 \quad (30)$$

The orientation nonlinearity introduced by α_1 can increase the frequency of sign changes from four to eight. Eqn.(30) embodies the orientation-driven first normal stress sign change mechanism (ONSC), shown in Figure 13.

In the flow-alignment regime, eqn.(28) becomes:

$$\lim_{E > E_{STFA}} N_1 = N_{1al} = \dot{\gamma} \left(\gamma_2 - \frac{\alpha_1}{\lambda} \right) \frac{\sqrt{\lambda^2 - 1}}{2\lambda} \quad (31)$$

and is proportional to the shear rate. Shearing a LC, with an heterogeneous director field and sufficiently high material nonlinearity (i.e; large $|\alpha_1|$), at increasing rates, will narrow and shift the orientation distribution function towards the Leslie angle, an orientation process that causes N_1 to change sign [54]:

$$N_1(\mathbf{n}_1(x), Er_1) < 0 \quad \rightarrow \quad N_1(\mathbf{n}_2(x), Er_2 > Er_1) > 0 \quad (32)$$

2.3. Landau de Gennes Nematodynamics

2.3.1. *Bulk and Interfacial Equations*

The governing equations for liquid crystal flows follow from the dissipation function Δ [26–31]:

$$\Delta = \mathbf{t}^s : \mathbf{A} + ck\mathbf{TH} : \hat{\mathbf{Q}} \quad (33)$$

where \mathbf{t}^s is the viscoelastic stress tensor, \mathbf{H} is the dimensionless molecular field, and $\hat{\mathbf{Q}}$ is the Jaumann derivative of the tensor order parameter. The molecular field \mathbf{H} is the negative of the variational derivative of the free energy density f :

$$f/ckT = \frac{1}{2} \left(1 - \frac{1}{3} U \right) \mathbf{Q} : \mathbf{Q} - \frac{1}{3} U \mathbf{Q} : (\mathbf{Q} \cdot \mathbf{Q}) + \frac{1}{4} U (\mathbf{Q} : \mathbf{Q})^2 + \frac{L_1}{2ckT} \nabla \mathbf{Q} : (\nabla \mathbf{Q})^T + \frac{L_2}{2ckT} (\nabla \cdot \mathbf{Q}) \cdot (\nabla \cdot \mathbf{Q}) \quad (34)$$

where the first line is the homogeneous (f_h) and the second the gradient (f_g) contribution; $U=3T^*/T$ is the nematic potential, T^* is the isotropic-nematic transition temperature, L_1 and L_2 are the Landau coefficients, and the superscript [s] denotes symmetric and traceless. In this format, comparing eqns.(12,34) gives $L_1=K_{22}/2S^2$, $L_2=K-K_{22}/S^2$, and $K=K_{11}=K_{33}$. The presence of the homogeneous energy allows the resolution of defect cores and the prediction of defect nucleation and coarsening. Expanding the forces ($\mathbf{t}^s, \hat{\mathbf{Q}}$) in terms of fluxes ($\mathbf{A}, ck\mathbf{TH}$), and taking into account thermodynamic restrictions and the symmetry and tracelessness of the forces and fluxes we can obtain the equations for \mathbf{t}^s and $\hat{\mathbf{Q}}$. The dynamics of the tensor order parameter is given by

$$Er \hat{\mathbf{Q}}^* = Er \left[\frac{2}{3} \beta \mathbf{A}^* + \beta \left[\mathbf{A}^* \cdot \mathbf{Q} + \mathbf{Q} \cdot \mathbf{A}^* - \frac{2}{3} (\mathbf{A}^* : \mathbf{Q}) \mathbf{I} \right] - \frac{1}{2} \beta \left[\begin{array}{l} (\mathbf{A}^* : \mathbf{Q}) \mathbf{Q} + \mathbf{A}^* \cdot \mathbf{Q} \cdot \mathbf{Q} + \mathbf{Q} \cdot \mathbf{A}^* \cdot \mathbf{Q} + \\ \mathbf{Q} \cdot \mathbf{Q} \cdot \mathbf{A}^* - \{ (\mathbf{Q} \cdot \mathbf{Q}) : \mathbf{A}^* \} \mathbf{I} \end{array} \right] \right] - \frac{3}{U} \cdot \frac{\square}{(1-\frac{3}{2} \mathbf{Q} : \mathbf{Q})^2} \left[\begin{array}{l} \left(1 - \frac{1}{3} U \right) \mathbf{Q} - U \mathbf{Q} \cdot \mathbf{Q} + \\ U \left\{ (\mathbf{Q} : \mathbf{Q}) \mathbf{Q} + \frac{1}{3} (\mathbf{Q} : \mathbf{Q}) \mathbf{I} \right\} \end{array} \right] + \frac{3}{(1-\frac{3}{2} \mathbf{Q} : \mathbf{Q})^2} \left[\begin{array}{l} \nabla^{*2} \mathbf{Q} + \frac{1}{2} L_2^* \left[\nabla^* (\nabla^* \cdot \mathbf{Q}) + \{ \nabla^* (\nabla^* \cdot \mathbf{Q}) \}^T \right] - \\ \frac{2}{3} \text{tr} \{ \nabla^* (\nabla^* \cdot \mathbf{Q}) \} \mathbf{I} \end{array} \right] \quad (35)$$

where: $\mathbf{t}^* = \dot{\gamma} \mathbf{t}$, $\mathbf{A}^* = \mathbf{A} / \dot{\gamma}$, $\mathbf{W}^* = \mathbf{W} / \dot{\gamma}$, $\nabla^* = H \nabla$, $L_2^* = L_2 / L_1$, β is a shape parameter, and $\dot{\gamma}$ is a characteristic shear rate. The first brackets denotes flow-induced orientation, the second phase ordering, and the third gradient elasticity.

The total extra stress tensor \mathbf{t}^t for liquid crystalline materials is given by the sum of symmetric viscoelastic stress tensor \mathbf{t}^s , anti-symmetric stress tensor, and Ericksen stress tensor \mathbf{t}^{Er} [54]:

$$\mathbf{t}^t = \mathbf{t}^s + \mathbf{t}^a + \mathbf{t}^{Er} \quad (36)$$

Summing up all the contributions and nondimensionalising we find:

$$\begin{aligned} \tilde{\mathbf{t}}^t = & \frac{Er}{\square} \left(v_1^* \mathbf{A}^* + v_2^* \left\{ \mathbf{Q} \cdot \mathbf{A}^* + \mathbf{A}^* \cdot \mathbf{Q} - \frac{2}{3} (\mathbf{Q} : \mathbf{A}^*) \mathbf{I} \right\} \right) + \\ & \frac{Er}{\square} \left(v_4^* \left[(\mathbf{A}^* : \mathbf{Q}) \mathbf{Q} + \mathbf{A}^* \cdot \mathbf{Q} \cdot \mathbf{Q} + \mathbf{Q} \cdot \mathbf{A}^* \cdot \mathbf{Q} + \right. \right. \\ & \left. \left. \mathbf{Q} \cdot \mathbf{Q} \cdot \mathbf{A}^* - \{ (\mathbf{Q} \cdot \mathbf{Q}) : \mathbf{A}^* \} \mathbf{I} \right] \right) + \\ & \frac{3}{U} \left[-\frac{2}{3} \beta \mathbf{H} - \beta \left\{ \mathbf{H} \cdot \mathbf{Q} + \mathbf{Q} \cdot \mathbf{H} - \frac{2}{3} (\mathbf{H} : \mathbf{Q}) \mathbf{I} \right\} \right] + \\ & \frac{3}{2U} \beta \left[(\mathbf{H} : \mathbf{Q}) \mathbf{Q} + \mathbf{H} \cdot \mathbf{Q} \cdot \mathbf{Q} + \mathbf{Q} \cdot \mathbf{H} \cdot \mathbf{Q} + \right. \\ & \left. \mathbf{Q} \cdot \mathbf{Q} \cdot \mathbf{H} - \{ (\mathbf{Q} \cdot \mathbf{Q}) : \mathbf{H} \} \mathbf{I} \right] + \\ & \frac{3}{U} (\mathbf{H} \cdot \mathbf{Q} - \mathbf{Q} \cdot \mathbf{H}) + \frac{3}{R} \left[\frac{-\nabla^* \mathbf{Q} : (\nabla^* \mathbf{Q})^T -}{L_1} \right. \\ & \left. \frac{L_2}{L_1} (\nabla^* \cdot \mathbf{Q}) \cdot (\nabla^* \mathbf{Q})^T \right] \end{aligned} \quad (37)$$

where

$$\tilde{\mathbf{t}}^t = \frac{\mathbf{t}^t}{ckT^*}, \quad v_1^* = \frac{v_1 6D_r}{ckT^*}, \quad v_2^* = \frac{v_2 6D_r}{ckT^*}, \quad v_4^* = \frac{v_4 6D_r}{ckT^*} \quad (38)$$

The total dimensionless extra stress tensor (38) is neither symmetric nor traceless. In this model there are three viscosity coefficients. The term introduced by β indicates back-flow. The term $\mathbf{H} \cdot \mathbf{Q} \cdot \mathbf{Q} \cdot \mathbf{H}$ is the asymmetric stress and the last is the purely elastic Ericksen stress.

The boundary conditions at fixed surfaces are obtained from the LdG interfacial nematodynamics [10, 56-58]:

$$\beta_s \frac{\partial \mathbf{Q}}{\partial t} = - \left\{ \left(\frac{\partial \gamma}{\partial \mathbf{Q}} \right)^{[s]} + \left(\nabla_s \cdot \left(\mathbf{I}_s \cdot \frac{\partial \gamma}{\partial \nabla_s \mathbf{Q}} \right) \right)^{[s]} \right\} - \left(\mathbf{k} \cdot \frac{\partial f_g}{\partial \nabla \mathbf{Q}} \right)^{[s]} \quad (39)$$

where β_s is a surface viscosity. Equation (39) states that the interfacial rate of change of \mathbf{Q} is given by the sum of the interfacial molecular field (first bracket) and the bulk gradient torques impressed onto the surface (second bracket). Under strong anchoring surface energy is minimized, and the preferred order parameter is the value of \mathbf{Q} that minimizes $(\partial\gamma/\partial\mathbf{Q})^{[s]}$. In the LdG model the surface energy γ is [12]:

$$\gamma = \left\{ \gamma_o + z_{11} \mathbf{k}\mathbf{k} : \mathbf{Q} + z_{21} \mathbf{Q}\mathbf{k}\cdot\mathbf{Q}\mathbf{k} + z_{22} (\mathbf{k}\mathbf{k} : \mathbf{Q})^2 \right\} + \left\{ \frac{L_{24}}{2} \mathbf{k}\cdot(\mathbf{Q} : \nabla_s \mathbf{Q} - \mathbf{Q}\cdot\nabla_s \cdot \mathbf{Q}) \right\} \quad (40)$$

where z_{ij} are anchoring coefficients and L_{24} is the saddle splay coefficient. The first bracket is the homogeneous and the second the gradient contributions. In the absence of surface gradients a useful one parameter surface energy is:

$$\gamma = \gamma_o + \frac{Z}{2} (\mathbf{Q} - \mathbf{Q}_o)^2 \quad (41)$$

where \mathbf{Q}_o is the preferred order parameter that minimizes γ .

2.3.2. Rheological Predictions

Projecting the LdG into the LE model we find the six Leslie coefficients [54]:

$$\begin{aligned} \alpha_1 &= \bar{\eta} \left(2\nu_4^* S^2 - \beta^2 S^2 \left(\frac{8}{9} - \frac{8}{9} S + \frac{S^2}{12} \right) \right) \\ \alpha_2 &= \bar{\eta} \left(-S^2 - \frac{1}{3} \beta S (2 + S - \frac{S^2}{2}) \right) \\ \alpha_3 &= \bar{\eta} \left(S^2 - \frac{1}{3} \beta S (2 + S - \frac{S^2}{2}) \right) \\ \alpha_4 &= \bar{\eta} \left(\nu_1^* - \frac{2}{3} \nu_2^* S + \frac{1}{3} \nu_4^* S^2 + \frac{4}{9} \beta^2 (1 - S - \frac{S^2}{4}) \right) \\ \alpha_5 &= \bar{\eta} \left(\nu_2^* S + \frac{1}{3} \beta S (2 + S - \frac{1}{2} S^2) + \frac{1}{3} \beta^2 S (4 - S - S^2) \right) \\ \alpha_6 &= \bar{\eta} \left(\nu_2^* S - \frac{1}{3} \beta S (2 + S - \frac{1}{2} S^2) + \frac{1}{3} \beta^2 S (4 - S - S^2) \right) \end{aligned} \quad (42)$$

where $\bar{\eta} = ckT^*/6D_r$. According to experimental data on rod-like nematics, the Miesowicz viscosities are connected as follows [70]:

$$\eta_1 + \eta_2 + 8\eta_3 = C_1 + C_2 (\eta_1 - \eta_2) \quad (43)$$

where C_1 is a constant and C_2 is bounded by : $2.77 < C_2 < 3.84$. Available molecular theories, such as the Doi and Hess models can replicate the experimentally observed rheological relation given by eqn.(43) only when using unphysical parametric values, such as $\lambda < 0$ for rods. In the present model, if we only retain linear terms in S in eqns. (42) we find that:

$$C_2 = \frac{8\beta^2 + 16v_2^*}{v_2^* + 4\beta} \quad (44)$$

For aligning rods ($\beta > 6/5$) the linearized model is consistent with experiments if $v_2^* > 0.57$. Expressions (42) allows us to express the reactive parameter λ , the shear viscosities ((η_1, η_2, η_3)), the normal stress difference N_1 in terms of the scalar order parameter S . For example the reactive parameter is [54]:

$$\lambda = \frac{\beta(4 + 2S - S^2)}{6S} \quad (45)$$

Rods will always align if $\beta > 6/5$ and disks if $\beta < 6/5$. In this model β is interpreted in terms of the geometry of the rheological flowing unit. For $De < 1$, the predictions are obtained by replacing S by its equilibrium value S_{eq} :

$$S_{eq} = \frac{1}{4} + \frac{3}{4} \sqrt{1 - \frac{8}{3U}} \quad (46)$$

For $De \gg 1$ numerical solutions are required. In this regime the Carreau-Yasuda model reads [54]:

$$\eta_s = \frac{\eta - \eta_\infty}{\eta_{al} - \eta_\infty} = \left[1 + (\tau \text{Er})^a \right]^{\frac{n-1}{a}} \quad (47)$$

where η_∞ is the plateau viscosity when S is close to one, and the parameters τ , a , n refer to the $De \gg 1$ regime. Hence the LdG model predicts a viscosity curve with three plateaus and two shear thinning regions [54].

As shown in [71] the LdG model emerges from the Doi-Hess molecular model based on the extended Maier-Saupe potential. For further discussions of the Doi-Hess molecular model, related nematodynamic models and rheological applications see [12,13,72-80].

3. DEFECTS AND TEXTURES

3.1. Defects in Nematics

Defects in NLC are classified into singular and non-singular [1, 2, 23, 81-84]. Singular defects include point and edge and twist disclination lines; the quantized strength of a disclination line $M (\pm 1/2, \pm 1, \pm 3/2, \dots)$ describes the amount of director rotation when encircling the defect. Singular disclination lines either form loops or end at other defects or bounding surfaces. Since the elastic energy of a defect scales with M^2 , the most abundant ones are the $M = \pm 1/2$. In the LdG model the cores of singular disclination lines correspond to unstable saddles of eqn.(48) and singular points correspond to unstable nodes [20,21,85]. Figure 14 shows a schematic of the stable (sink) uniaxial nematic root ($S=S_{eq}, P=0$), the unstable (source) defect point ($S=P=0$) and the unstable (saddle) disclination line, which are the roots of:

$$\left(1 - \frac{1}{3}U\right)\mathbf{Q} - U\mathbf{Q} \cdot \mathbf{Q} + U \left\{ (\mathbf{Q} : \mathbf{Q})\mathbf{Q} + \frac{1}{3}(\mathbf{Q} : \mathbf{Q}) \mathbf{I} \right\} = 0 \quad (48)$$

In addition to singular defects, non-singular defects arise in the form of lines and inversion walls [1,2,8-84,86]. Non-singular defects are captured by the LE model since they do not involve changes in the order parameters. Nonsingular disclination lines appear to minimize the energy through out-of-plane director escape, thus avoiding orientation singularities. Inversion walls appear in the presence of external fields, when the field-induced orientation has a degeneracy such that clockwise and anti-clockwise rotations are equally possible.

CM/carbon fiber composites offer a spectacular example of singular and non-

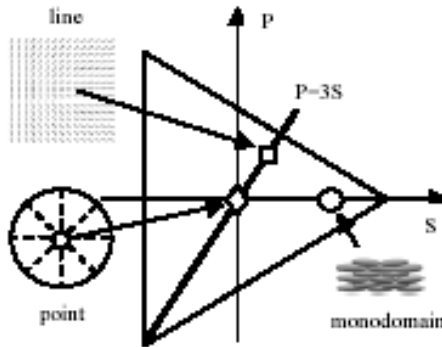


Figure 14. Schematic of stable and unstable roots of the free energy (eqn.(48)). Defect free monodomain (circle) is a stable root, the point defect (diamond) is an unstable node, and the disclination line is an unstable saddle.

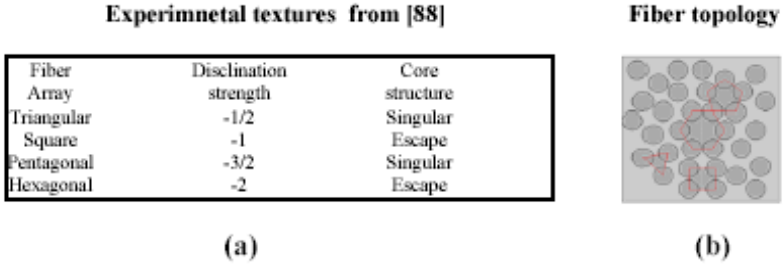


Figure 15. (a) Table of observed disclinations in carbon/carbon composites. (b) schematic of carbon/carbon composites; the matrix is a CM and the circles are the carbon fiber cross-sections. Adapted from Ref. [87,88].

singular disclination lines in a liquid crystal fiber composite system [87,88]. Experiments and topology show that when filling a CM with a parallel array of cylindrical micron sized carbon fibers with their axis normal to the director, a random lattice of disclination lines emerges in the liquid crystalline matrix. Figure 15 shows a table with the disclination line types observed experimentally and predicted by simulations (left table) and a schematic of the random fiber arrangement with triangular, square, pentagonal, and hexagonal arrangements (right figure); the fiber arrangements are indicated by the closed polygons. The topological rule, derived using the Poincare-Brower theorem of differential geometry, that relates the fiber arrangement N and the disclination strength M is $M = -(N-2)/2$. For example when the fiber arrangement is triangular and $N=3$, the disclination charge is $M = -(3-2)/2 = -1/2$ and when the fiber arrangement is hexagonal and $N=6$ the charge is $M = -(6-2)/2 = -2$. The sign means that the net charge associated with the fibers is positive and hence the disclinations have to have negative charge. In addition to the charge associated with the fiber arrangements, the core type is also affected, such that a distinct even and odd effect arises.

Odd fiber arrangements lead to singular cores while even fiber arrangements lead to non-singular cores [87,88]. Odd fiber arrangements lead to singular disclination lines since director escape into the third dimension is blocked by symmetry and since $M = -1/2$ lines are stable because there is no topological transformation that eliminates them. Figure 16 shows the arrangement predicted by the LdG nematostatic model for $N=3$ (a) and the director orientation associated with a disclination line $M = -1/2$ shown on the unit sphere (b). Figure 16a shows the director field and the scalar order parameter (high S is light and low S is dark); at the center of the fiber triangle there is a singular disclination of charge $-1/2$, shown by the dark dot. Figure 16b shows the director orientation around the disclination line and the path (closed circle with arrow) over which the director rotates π radians. Figure 16c shows that for a $M = -1/2$ the director is a path connecting two poles and there is no topological transformation that can be used to eliminate the singularity.

According to Figure 15 even fiber arrangements lead to escape disclination lines. For example, when $N=4$, the total charge observed is $M = -1$. Since singular lines

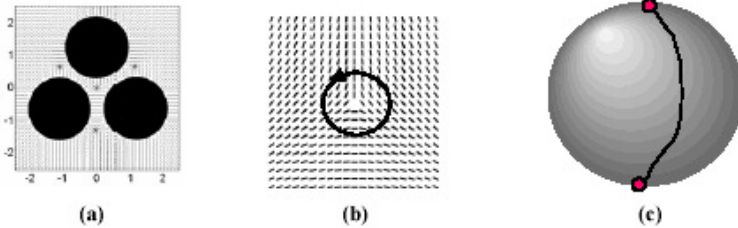


Figure 16. (a) Singular $M=-1/2$ disclination at center of $N=3$ fibers. (b) Schematic of the $M=-1/2$ disclination line. (c) North-to-south pole trajectory that describes the director orientation when encircling the line shown in (b).

of strength $M=-1$ are unstable to perturbations of the director along the third direction the singular core does not emerge and instead a micron-range core emerges within which the director rotates out-of-plane.

Figure 17a shows a LdG prediction for a $N=4$ arrangement with an escape $M=-1$ non-singular line. Figure 17 b shows the topological transformation that leads to the removal of the singular line and its replacement with a nonsingular one; The top Figure 17b (left) is the orientation sphere with the director equatorial trajectory associated with a singular line shown below the sphere. Figure 17b shows how the singular line can be removed by smoothly pulling the equatorial trajectory towards the north pole. Integral disclination lines are unstable since a loop on the unit sphere can

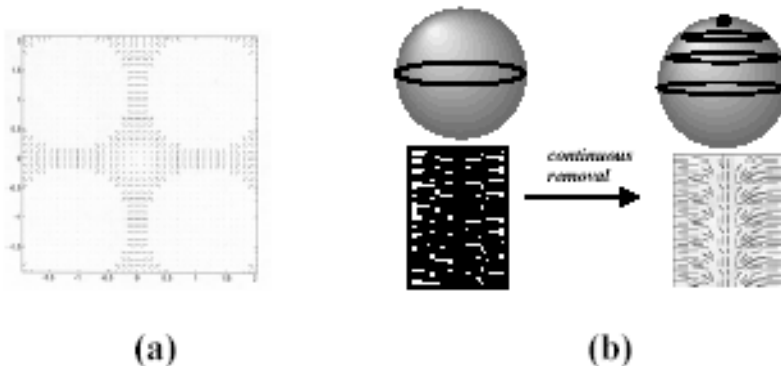


Figure 17. (a) Nonsingular $M=-1$ disclination line. (a) Topological transformation showing the instability of integer singular lines: the singularity (loop on the equator of the orientation unit sphere) is eliminated by sliding it out of the sphere.

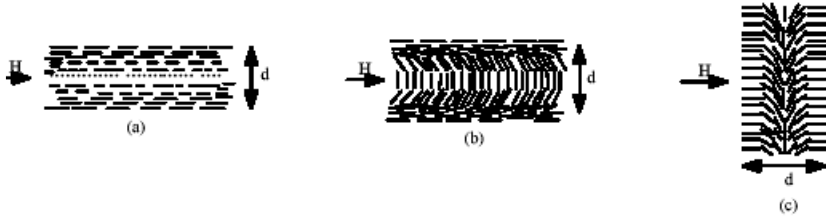


Figure 18. Director patterns in (a) twist, (b) bend, and (c) splay inversion walls created by the presence of an orienting external field H.

slide off leaving behind a uniform orientation.

Non-singular orientation wall defects are 2D defects that may arise under the presence of external fields, such as flow fields and electromagnetic field [1,2]. Figure 18 shows the director pattern around twist (a), bend (b) and splay (c) inversion wall defects created by the external field H. The elastic energy per unit area or surface tension stored in a wall of thickness d is K/d .

A rheological example of flow-induced inversion wall formation arises in the spinning of CMs through ribbon-shaped dies, shown in Figure 19 [89,90]. At low deformation rates the fiber cross-section exhibits a line defect (a), but as the deformation rate increases the upper half sector rotates clockwise while the bottom half rotates anticlockwise giving rise to a 2D non-singular inversion wall; see thick black line in Figure 19 (b). In this case viscous torques are such that the director is aligned along the compression direction (horizontal axis in Figure 19), which can be reached by rotating along the fiber axis (direction into the page in Figure 19) in either sense. A 1D analysis based on the LE nematodynamics for planar extensional flow of CMs, gives the planar director angle $\theta(y)$ as a function of the vertical y coordinates as:

$$\tan\left(\frac{\theta}{2}\right) = \exp\left\{-\frac{y}{H}\sqrt{E_r}\right\} \quad (49)$$

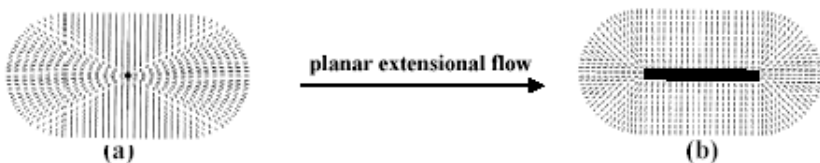


Figure 19. (a) Director orientation on a ribbon-shaped CM fiber at low planar extensional flow deformation rate. (b) Ribbon-shaped CM fiber at high planar extensional flow deformation showing an inversion wall at the centerline (thick line). Adapted from Ref. [89].

where H is the vertical fiber thickness and y is the vertical direction in Figure 19.

Equation (49) describes an inversion wall solution that is in excellent agreement with experiments [89,90]: for $y \gg H/\sqrt{E_r}, \theta \rightarrow 0$ and $y \gg -H/\sqrt{E_r}, \theta \rightarrow \pi$ and in the centerline region there is a rapid rotation between these two angles ($\theta = 0$ and $\theta = \pi$). Next we discuss point and line defect phenomena mainly in reference to CMs.

3.1.1. Point Defects

Point defects are singular solutions to the static LE equations in spherical coordinates [1,2, 82, 91]. Figure 20 shows schematics of a radial and hyperbolic points defects of strength $M=+1$.

The charge M_p of a point defect is defined by [91]:

$$M_p = \frac{1}{8\pi} \iint d\mathbf{S} \cdot \boldsymbol{\varepsilon} : (\nabla \mathbf{n} \times \nabla \mathbf{n}) \cdot \mathbf{n} \quad (50)$$

which indicates that radial and hyperbolic points defects carry the same charge and can be transformed into each other continuously. In nematics the combined charge of two point defects is either $M_p = |M_{p1} - M_{p2}|$ or $M_p = |M_{p1} + M_{p2}|$ and hence different outcomes are possible for the reaction of two points. The director energies associated with these bulk point defects are $E_{\text{radial}} = 8\pi KR < E_{\text{hyper}} = 8\pi KR/3$. Point defects appear in the formation of CMs through nucleation, growth and impingement of nematic spherulites. For planar director orientation point defects appear on the surface of the spherulite. According to differential geometry the Euler characteristic of a surface χ is the average Gaussian curvature K ($K = (1/R_1)(1/R_2)$; $R_{1,2}$: radius of curvature) and for a sphere of radius R the Euler characteristic is [92] :

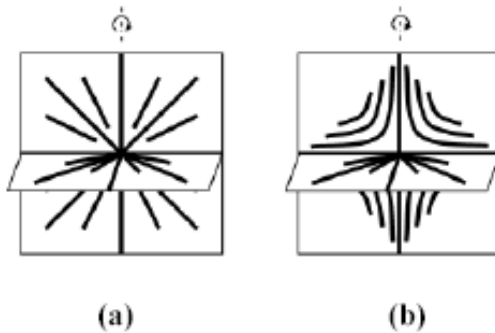


Figure 20. Schematic of a radial +1 (a) and a hyperbolic (b) +1 point defect.

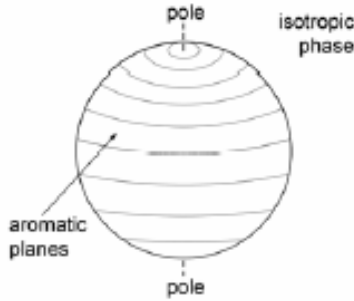


Figure 21. Schematic of the Brooks and Taylor nematic spherulite. At the poles there is a +1 defect point and the surface orientation is edge-on. Adapted from Ref. [44].

$$\chi = \frac{1}{2\pi} \iint \frac{1}{R^2} dS = 2 \quad (51)$$

According to the Poincare-Brouwer theorem mentioned above, the total charge (i.e. strength of the singularities) of a vector field on a surface is equal to the Euler characteristic of the surface [92]. This theorem can then be used to predict surface defects on nematic liquid crystals. For tangential surface orientation, the theorem predicts that a nematic spherulite has a total charge of surface defects of +2. For CM spherulites, Brooks and Taylor [44] found that for spherulites in the micron range two defect points of charge +1 each at the poles are observed, as indicated in Figure 21, in agreement with the prediction of the Poincare-Brouwer theorem. Using the static LE model with $K_{24}=0$ and elastic isotropy, it is shown [92] that the elastic energy associated with the director field of a Brooks and Taylor spherulite of radius R is $E=5\pi KR$ and is less than the spherulite with a +1 defect at the center of the sphere with $E=8\pi KR$.

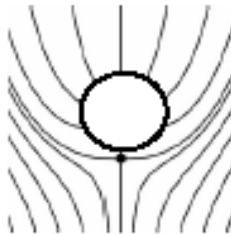


Figure 22. Schematic of director trajectories around a bubble-defect point dipole. The large circle is the bubble and the dark point is the defect.

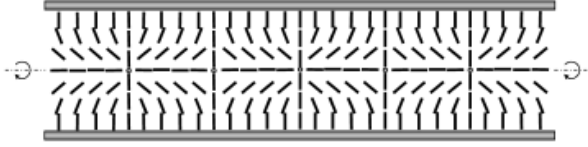


Figure 23. Schematic of a NLC confined in a capillary, displaying a periodic array of +1 and -1 point defects along its axis. This texture is known as escaped radial with point defects, ERPD.

Point defects may also play a role during the mesophase formation when gaseous bubbles exist from the system [23]. For large enough bubbles we can expect a dipole arrangement in which the bubble form a stable configuration with a -1 point defect. In such case it is known that there is an equilibrium distance between the point defect and the bubble of radius R at which repulsive and attractive force equilibrate in the range of approximately 1.2 to 1.5 R . Stable dipole pairs containing -1 point defects and air bubbles have been found in rod-like NLCs. Figure 22 shows an schematic of the director field lines around a bubble-defect dipole. For CMs such as structure should arise in the presence of phase-on anchoring.

Point defects also arise under capillary confinement, as shown in Figure 23 [93,94]. For rod-like nematics in capillaries and homeotropic anchoring, a periodic array of alternating +1 and -1 point defects along the axis are usually observed; the defect-defect separation distance is of the order of the capillary radius. This texture form when the escape mechanism is selected but since clockwise and anticlockwise escape is possible defect point arise. This metastable texture is known as escape radial with point defects (ERPD). Hence we would expect that for CMs under capillary confinement a similar periodic point defect texture may arise.

In general texturing due to confinement requires that the characteristic system size H be greater than the extrapolation length ℓ_{extra} :

$$\ell_{extra} = \frac{K}{\gamma_2} \ll H \quad (52)$$

and in principle for a given LC this length can be changed by modifying the interface.

Point defects have another aspect of interest to the understanding of texturing processes. Figure 24a shows the connection between points defects and disclination loops, given in terms of director trajectories. The figure shows that a radial defect point is equivalent to a - 1/2 disclination loop and that a hyperbolic defect point is equivalent to a 1/2 disclination loop. Figure 24b shows the corresponding LdG computations of a defect loop at the center of a sphere; this figure and associated computations demonstrate that radial +1 points are disclination loops and that the radius of the loop is approximately 4-5 times the molecular length scale.

Given that point defect are disclination loops, the behavior of these loops under capillary confinement has implications to fiber textures and to topological transformations [93,94]. Consider the capillary confinement of a LC such as that

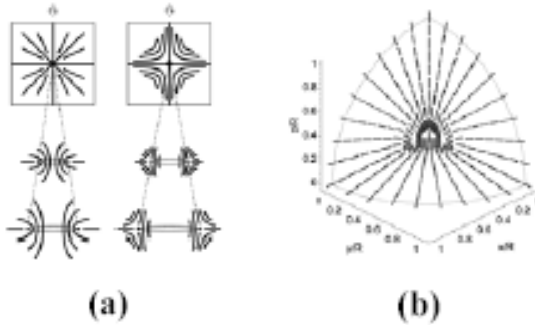


Figure 24. (a) Radial (hyperbolic) point defects are equivalent to $1/2(-1/2)$ disclination loops. (b) Computed \mathbf{Q} -tensor visualization at the center of a sphere: point defects are disclination loops; Adapted from Ref. [94].

shown in Figure 23. Since the points defects are loops, two topological processes are possible: (a) a disclination loop can expand and break into a pair of disclination lines, and (b) a loop can react with another loop to form a ring whose charge is the sum of the initial two loops. These two topological processes have implications in texture formation and stability in capillary geometries, filled nanotubes and fibers.

Figure 25 shows LdG static computations of how an initial radial disclination loop in a capillary grows into a distorted loop that eventually splits into a pair of $1/2$ disclination lines parallel to the capillary axis giving rise to the PPLD texture. The original disclination loop is stable at $U=6$ only of the capillary radius $R>21.5 \ell_i$. The originally circular disclination loop is oriented with its unit normal along the radial direction of the cylindrical capillary and the loop expansion axis is the axial z -coordinate. Once the lines form, they drift apart due to repulsive forces and settle at distance slightly larger than the fiber radius. The topological process under cylindrical

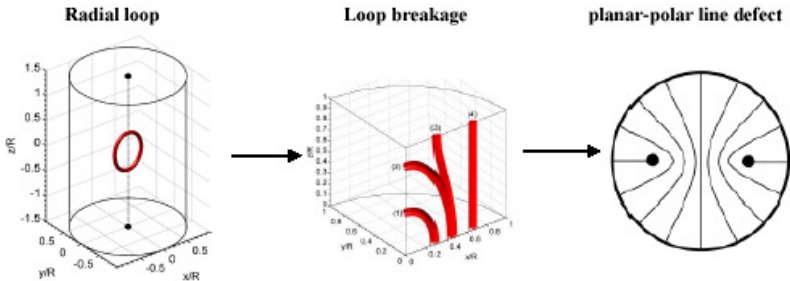


Figure 25. Topological transformation of a single defect loop into a pair of $1/2$ disclination lines parallel to the axis of the capillary, predicted by the LdG model. Adapted from Ref. [94].

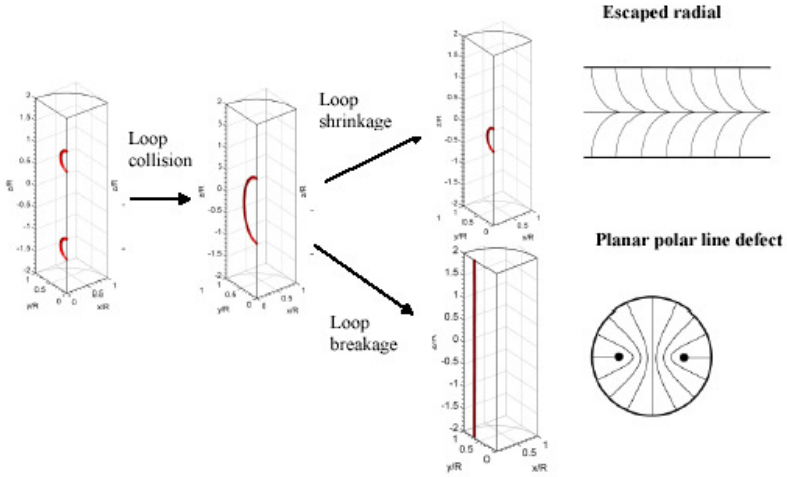


Figure 26. Computed topological transformations from a pair of radial and hyperbolic disclination loops into the escaped radial texture and planar polar line defect texture. Adapted from Ref. [93].

confinement is:

$$M_{loop} = +1 \rightarrow 2 M_{line} = +1/2 \quad (53)$$

The second topological process that can occur with disclination loops under capillary confinement involves loop-loop reactions [93]. Consider a texture with a periodic array of disclination loops of alternating charge. These metastable texture can evolve into other textures through loop-loop reactions and the resulting texture will inevitably depend on the size of the capillary. Figure 26 shows computed visualizations based on the LdG model of a radial and hyperbolic loop colliding due to their mutual attraction within a capillary to form a daughter loop whose radius is approximately the sum of the parent loop radii. The figure shows a quarter cylinder for better visualization. The daughter loop that results from the loop collision is shown on the second cylinder from the left.

The fate of the daughter loop is dictated by the radius of capillary R : when $R < 25\xi$ and $U=6$ the loop shrinks and the escaped texture emerges (top path in Figure 26), while if $R > 25\xi$ and $U=6$ the loop expands and breaks into a pair of $1/2$ disclination lines forming the planar polar line defect texture (bottom path in Figure 26).

3.1.2. Disclination Lines

Wedge and twist disclinations are possible according to the rotation axis: wedge (twist) lines are parallel (perpendicular) to the rotation axis [1,2,23]. Wedge

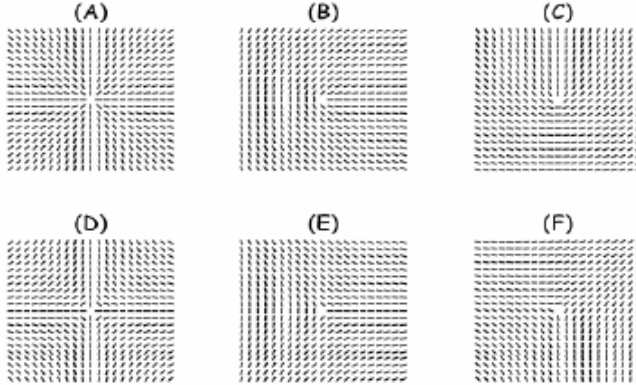


Figure 27. Director fields around singular wedge disclinations. (A) $M=+1$, (B) $M=+1/2$, (C) $M=+1/2$ and $\phi_0=\pi/4$, (D) $M=-1$, (E) $M=-1/2$, (F) $M=-1/2$ and $\phi_0=\pi/3$.

disclination lines are associated with planar orientation given by $\mathbf{n}=(\cos \varphi, \sin \varphi, 0)$, $\varphi=M\phi+\phi_0$, where φ is the director angle with respect to the x -direction, ϕ is the polar angle of a cylindrical coordinate system, M is the strength of the disclination and ϕ_0 is a constant that determines the overall orientation of the defect. Figure 27 shows director fields around typical singular wedge disclination lines.

Since defects have associated a core and distortion energy, short and long range energy calculations are used to establish their stability [84]. It turns out the defect energy is proportional to their strength squared and to the three Frank elastic constants (K_{11} , K_{22} , K_{33}) involved in the deformation associated with the disclination. Anisimov and Dzyaloshinskii (1972) showed that elastic anisotropy controls the stability of the different classes of disclinations, and thus the relative abundance of certain types of defects. For discotic nematics it is known that $K_{22}>K_{11}$, $K_{22}>K_{33}$. Furthermore it is expected that for low molar mass discotics $K_{11}>K_{33}$ and for larger molecular weight $K_{33}>K_{11}$ [95].

The effects of elastic anisotropy on the stability of $S=\pm 1/2$ lines are: (a) wedge disclinations are favored when $K_{22}>(K_{11}+K_{33})/2$, and are stable against out-of-plane perturbations; (b) twist disclinations are favored when $K_{22}<(K_{11}+K_{33})/2$, and are unstable against out-of-plane perturbations. As a consequence the predictions are that for discotic mesophases wedge disclinations of $S=\pm 1/2$ should be more abundant than twist disclinations of the same strength. Zimmer and White [23] report the existence of both.

For $S=1$ it is found [96] that the only stable wedge lines against out-of-plane perturbations are those with purely radial or azimuthal director orientation. Whether

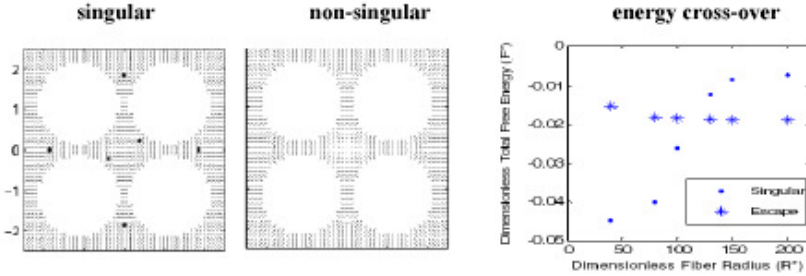


Figure 28. (a) Role of geometry on the core nature: larger(smaller) create non-singular (singular) lines. (b) Computed total free energy as a function of fiber radius, showing the cross-over from singular to non-singular cores, based on the LdG model. Adapted from Ref. [87].

these lines have singular or non-singular cores will depend on the degree of anisotropy, in the nature and size of the core and the confinement. For relatively weak elastic anisotropy it is expected that non-singular cores will prevail. The nature of the core in disclinations of unit strength have been characterized by Zimmer and White [23], and they show that $S = \pm 1$ lines have nonsingular cores in the bulk but discontinuous near free surfaces. As shown above for C/C composites made of mm sized fibers with a fiber arrangement of $N=4$, -1 non-singular lines are observed. Nevertheless we can expect that for submicron fibers two $-1/2$ singular disclinations have less energy than a single -1 non-singular line. Figure 28 shows computed visualizations of the director based on the LdG model ($U=3.5$, $L_2=0$) for submicron (left) and micron (right) sized fibers (a), and the corresponding total free energy (b), showing that when $H \approx 125\ell_1$ there is an energy cross-over; NB: here H stands for the fiber radius [87]. The simulations shows that even under elastic isotropy ($K_{11}=K_{22}=K_{33}$) the complex geometries present in random composites need careful analysis to ascertain the nature of the disclination cores.

The experimental data of Zimmer and White [23] conclusively shows that CMs display a defect phenomenology characteristic of other nematics and that their observations on defect types and defect cores can be well explained by the LdG equations.

3.2. Textures during Carbonaceous Mesophase Formation

During the isotropic-nematic mesophase phase transformation, when the spherules grow and coalesce to produce large mesophase regions, a large number of disclinations nucleate [23]. The nucleation of disclinations or texture formation occurs because a lack of orientation registry between the uncoalesced mesophase regions, such that when they come into contact, orientation incompatibility is resolved by the nucleation of disclinations. For example when three droplets coalesce a disclination of strength $S=+1/2$ results [23]. Figure 29 (a) shows an schematic of the Kibble mechanism for generation of disclination lines by droplet impingement and (b) shows

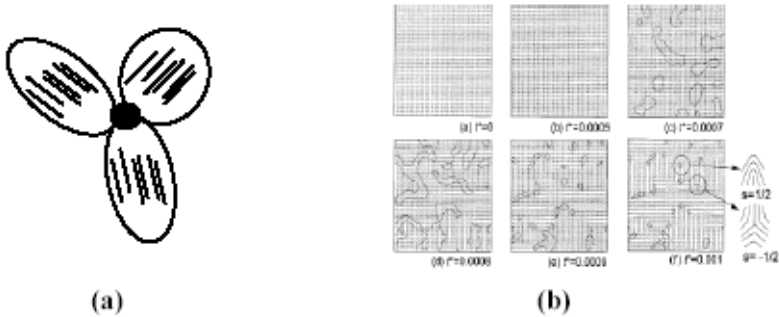


Figure 29. (a) Schematic of the Kibble mechanism of de-nucleation by droplet impingement. (b) Computed visualizations based on the LdG model of texture formation by the Kibble mechanism for increasing values of the energy ratio R . Adapted from Ref. [26].

computed optical visualizations based on the 2D LdG model for increasing values of the energy ratio R (eqn.(5)), showing how by decreasing the relative importance of gradient elasticity the texture coarsens [26].

Other concurrent mechanism already mentioned above are the presence of surface point defects on nematic spherulites and point defects associated with bubbles that result from the chemical reaction associated with mesophase formation. In addition, the low interfacial tension of the nematic-isotropic interface, typically of the order of 10^{-2} mN/m, is fertile ground for defect nucleation [10,60,61]. Indeed the LdG model predicts that as a nematic spherulite grows, interfacial heterogeneities invariably leads to nucleation of disclinations that are then emitted into the spherulite interior [97-100].

Figure 30 shows representative computed visualizations of defect nucleation in growing nematic spherulites. The figure shows that at the nematic (black with white segments for the director) interface with the isotropic (gray area) matrix the orientation is planar on the left and homeotropic on the right. Since planar (homeotropic) anchoring leads to biaxiality (uniaxiality) there is an interfacial discontinuity that leads to the nucleation of a disclination loop. The loop is emitted into the interior of the spherulite and eventually shrinks into a $1/2$ line. These prediction are difficult to detect because they occur at scales not accessible to most experimental detection techniques. To explain interface-driven texturing one must consider the governing shape equation. The interfacial liquid crystal dynamic shape equation (Eq.(54)) identifies how the stress load, capillary pressure, friction, and the surface viscosity can cause different normal interface velocities which leads to the cusp formation observed in interfacial defect shedding [97-100]:

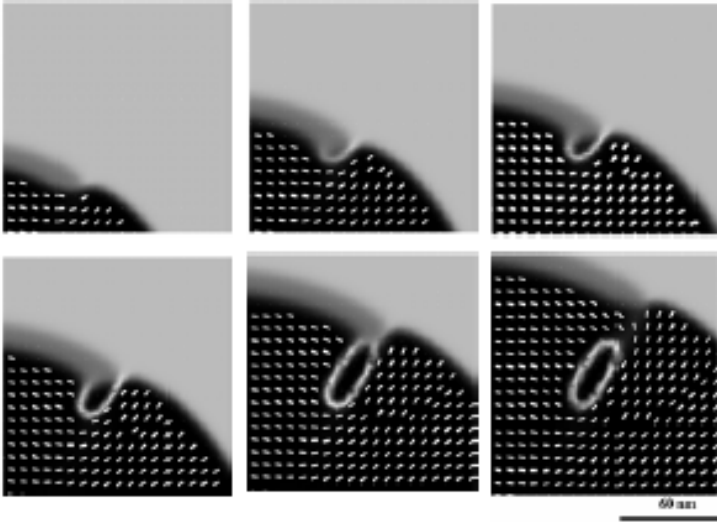


Figure 30. Computed visualizations of interfacial defect shedding in a growing nematic spherulite during the isotropic-to-nematic transition. Adapted from Ref. [98].

$$\beta_{\perp} w_{\perp} = \{ \mathbf{L} + \nabla_s \cdot \mathbf{T}_s \} \cdot \mathbf{k} + \beta \mathbf{Q}^s : \frac{d\mathbf{Q}^s}{dt} \quad (54)$$

where β_{\perp} is a surface viscosity, w_{\perp} is the normal interface velocity, \mathbf{L} is the net stress loading at the transverse boundaries, ∇_s is the surface gradient tensor, \mathbf{T}_s is the surface stress tensor, \mathbf{k} is the interface unit normal, \mathbf{Q} is the surface tensor order parameter, and β is the bulk rotational viscosity coefficient.

The cusps forms due to differential normal interface velocities w_{\perp} , i.e. when the normal interface velocity w_{\perp} is not identical at all points along the moving interface. As shown in Eq.(54), to characterize and explain the cusp formation process, it is necessary to analyze the terms that control the normal velocity w_{\perp} , which are: the load \mathbf{L} , the capillary pressure $(\nabla_s \cdot \mathbf{T}_s)$, the friction $\beta \mathbf{Q}^s : d\mathbf{Q}^s / dt$, and the surface viscosity β_{\perp} . An analysis of cusp formation done in previous work [100] suggests that away from the cusp, the normal interface velocity w_{\perp} is constant as the total stress load (\mathbf{L}) is just the free energy difference associated with the homogeneous isotropic/nematic phase transition, the surface viscosity (β_{\perp}) is constant and capillary

$(\nabla_s \cdot \mathbf{T}_s)$ and friction forces ($\beta \mathbf{Q}^s : d\mathbf{Q}^s / dt$) are negligible. Where the center of the cusp forms along the interface, all terms in Eq.(54) play a role and the surface viscosity appears to be changing transiently so that this part of the moving interface experiences first a slow deceleration, then a fast acceleration, and finally a fast deceleration to form the cusp. The slow deceleration creates the cusp, the fast acceleration nucleates the defect, and the fast deceleration sheds the defect.

3.3. Texture Coarsening

After a symmetry breaking phase transition the mesophase exhibits a texture, or distribution of defects of various strength. Textures undergo coarsening processes driven by defect-defect reactions and annihilations, defect recombinations that emit loops that shrink, among several possibilities [12]. Thus texture coarsening is driven by a defect density reduction. Texture coarsening is a self-similar process whose scaling law gives the relation between the mean defect separation distance ζ_d in a space of dimension d and time t as a power law: $\zeta_d \approx \rho(t)^{-1/d} \approx t^n$. Chuang et. al. [101] performed studies of the isotropic-rod-like nematic transition of 5CB by pressure quenches. Texture coarsening followed the self-similar process with the power law exponent $n=0.5$, as expected in dispersive systems.

Data on overall coarsening rates and power law exponents have not been measured for CMs. On the other hand the defect-defect reactions and annihilations that drive texture coarsening have been documented by Zimmer and White [23]. They report the observation of the following wedge disclination interactions:

$$M=+1 + M=-1/2 \Leftrightarrow M=+1/2$$

$$M=-1 + M=+1/2 \Leftrightarrow M=-1/2$$

$$M=+1/2 + M=-1/2 \Leftrightarrow 0$$

$$M=+1 + M=-1 \Leftrightarrow 0$$

$$M=+1/2 + M=+1/2 \Leftrightarrow M=+1$$

$$M=-1/2 + M=-1/2 \Leftrightarrow M=-1$$

These disclination reactions were observed on the free surface of a CM and are driven by elastic energy reduction. When the mesophase was quite fluid the recovery by defect annihilation was rapid. As the viscosity increased by continued pyrolysis leaving increasingly fine deformed microstructures in the hardening mesophase. They made the critical observation that deformation processes can be imposed on a CM well beyond the point at which disclinations interact significantly, explaining the relatively high densities of disclinations in carbon products.

Figure 31 shows the isotropic-to-CM transition in a circular domain of radius R ; the bottom is the director field and the top is the scalar order parameter S (dark denotes low order and light high nematic order). The times are scaled with the molecular time scale, $U=6$, $H/\ell_1=3.6$, and the surface anchoring is edge-on. The figure shows how the planar radial texture with an $M=+1$ disclination at the fiber axis

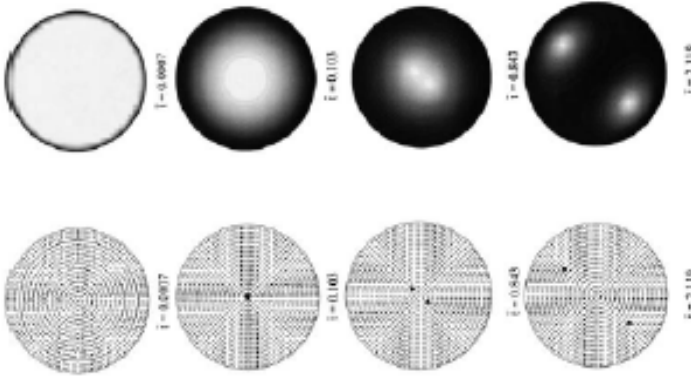


Figure 31. Computed visualizations of the scalar order param (top) and director (bottom) field showing the $M=+1 \rightarrow 2 M=-$ disclination line reaction. Adapted from Ref. [102].

forms first and then decays through a disclination reaction into a pair of $+1/2$ disclination lines. The splitting is driven by reduction of the energy E_{line} which is proportional to the square of the disclination charge M [1]:

$$E_{\text{line}} = E_{\text{core}} + \pi K M^2 \ln \left(\frac{H}{r_c} \right) \quad (55)$$

where E_{core} is the energy associated with the core, H is the fiber radius and r_c is in the nanoscale range.

Once the two $1/2$ lines nucleate they drift apart due to repulsive interactions, eventually setting at an equilibrium distance $L = H/\sqrt[4]{5}$ [52]. Figure 32a shows representative computed visualizations [102], based on the LdG model of CMs ($U=6$, $H/\ell_i = 31.6$), of a $M = +1/2 + M = -1/2 \Leftrightarrow 0$ annihilation, in a circular domain of radius R in the presence of two other $+1/2$ disclinations and Figure 32b shows the gradient energy as a function of time. The time is scaled with the molecular time scale

Figure 32 shows that in the nucleation stage II the three $+1/2$ and one $-1/2$ disclination arise, in the intermediate stage III the disclination rearrange, and in stage IV after annihilation the two remaining disclinations repel. Hence in the general case we can expect to have defect nucleation, defect-defect reactions, and a late stage with pinning.

Defect-defect annihilation drive coarsening processes that increase domain length scales [12,13,26,64]. Defect-defect annihilation is not completely characterized, and some not fully resolved questions are: (i) what is the role of hydrodynamic interactions or re-orientation induced flow, (ii) what is the role of neighboring defect on the annihilation of a defect pair (long range effects), and (iii) what is the role of

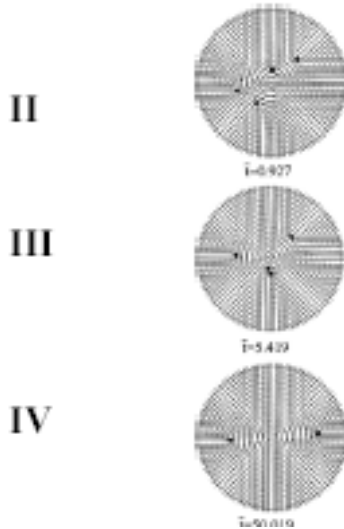


Figure 32. (a) Computed visualizations of defect nucleation, defect-defect annihilation ($M=1/2+M=-1/2 \rightarrow M=0$), and defect texture. The initial increase due to defect nucleation followed by decrease driven by annihilation. Adapted from [102].

elastic anisotropies. Here we briefly focus on the second issue regarding long range effects [103]. Explorations of $M=1,-1$ defect-defect annihilations in the presence of other disclinations under capillary confinement have been performed with a variable director length LE model.

This variable director length model allows to approximate singular disclinations of integral strength. Figure 33a shows computed visualizations at three times for a sequence of $-1,+1,-1$ point defects along the axis of a capillary of circular cross-section, where the top pair annihilates in the presence of the third -1 defect. The issue of how sensitive is the perturbation due to the presence of the third defect is answered in Figure 33b, where the same simulations as in Figure 33a were performed using the location of the bottom -1 defect as parameter. Figure 33b shows the defect trajectories as a function of time; when two neighboring trajectories merge, it denotes that the defect pair has annihilated. Figure 33b shows that as the third defect moves closer to the upper pair (vertical arrow) the annihilation dynamics of the pair slows down (horizontal arrow) as well as the symmetry is broken, such that annihilation does not occur at the midpoint. Figure 33c shows collective modes of many defect pairs, where large variability, sometimes by a factor of five, on annihilation times are observed. In addition, the figure shows that there is always a likelihood of remaining defects due to

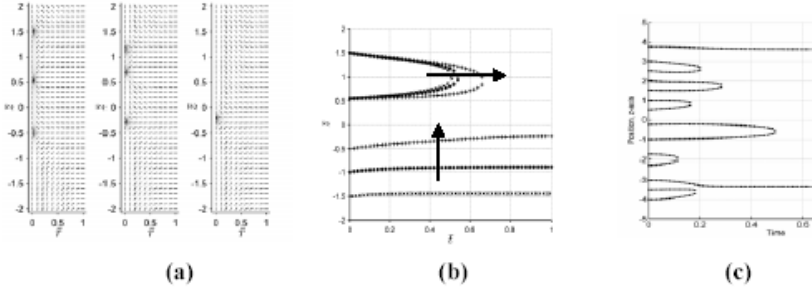


Figure 33. (a) Computed visualizations of a point defect annihilation in the presence of a third one at three increase times. (b) Effect of a single defect on the dynamics annihilation of a defect pair: moving the defect closer to reacting pair slows the dynamics. (c) High variability annihilation times due to collective mode behavior. Adapted from Ref. [103].

the fact under capillary confinement the interaction force is vanishingly small when the defect-defect distance is larger than the radius of the capillary.

3.4. Defect Rheo-Physics

In this section we discuss some fundamental concepts necessary to characterize defects and textures in sheared flow-aligning LCs and CMs.

3.4.1. Defect Nucleation Processes

Flow-induced defect nucleation in non-aligning lyotropic LCPs is associated with the lack of steady flow-alignment and the presence of spatial gradients of rotational director kinetics [26]. Two neighboring regions whose average molecular orientation rotate at different speeds will create interfacial gradients that will be compatibilized by defect nucleation. Flow-induced defect nucleation in flow-aligning LCs is not associated with tumbling processes as in sheared non-aligning LCs, since the latter tend to align within the shear plane and close to the shear flow direction at an angle known as the Leslie angle θ_L (see eqn.(13)). On the other hand other shear-induced processes can clearly lead to defect nucleation in flow-aligning LCs, including [53]: (1) defect loop emission by the Frank-Reed surface mechanism [104], (2) stretching and pinching of existing loops in the bulk, and (3) heterogeneous reorientation upon flow-start-up. Direct numerical simulation of all these three co-existing nucleation processes for flow-aligning LCs is beyond existing computational power since the ratio of a defect core to typical shear cell sizes (the energy ratio \square in eqn.(5)) is at least five or more orders of magnitude. This critical limitation fuels the motivation of using simplified models and theoretical frameworks that provide

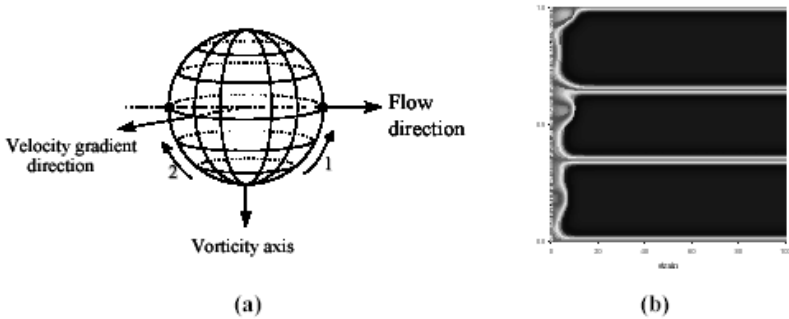


Figure 34. (a) The reorientation from vorticity to flow-alignment can proceed along two equivalent paths. (b) Visualization of the resulting inversion walls : the dark are flow-aligned regions and the light are aligned along the vorticity. Adapted from Ref. [105].

insights to texture transformations. In previous work, the loop emission process [104] and its impact on rheology was investigated. One of the simplest defect nucleation mechanisms for shear flow-aligning LCs is due to heterogeneous re-orientation process, shown in Figure 34 for CMs [105]. For orientation along the vorticity there are two equally probable paths to the flow-alignment state, which result in the formation of inversion wall defects, visualized in Figure 34b, where the dark refer to the director close to the velocity gradient and the light denote orientation along the vorticity. The simulations show that shearing a randomly oriented sample will invariably lead to texturing even if the material is flow-aligning.

Numerical simulations indicate that the defect nucleation rate $\dot{\rho}$ for $\dot{\rho} = 10^4$ - 10^6 are well fitted by a power law model [53]:

$$\dot{\rho} \approx 0.01 \Upsilon(Er - Er_{ADL}) \sqrt{Er - Er_{ADL}} \quad (56)$$

where Υ is the Heaviside function and $Er_{ADL} = 9 \times 10^4$ (for $R = 10^5$) is the minimum Erisken number for defect nucleation. The length scale of the texture $\ell_t = H/\dot{\rho}$ is given by [54]:

$$\ell_t = \frac{H}{c \Upsilon(Er - Er_{ADL}) \sqrt{Er - Er_{ADL}}} \quad (57)$$

where c is a constant and H is the system size. Thus in the absence of coarsening the texture length scale predicted by LdG decreases with a $-1/2$ power law [53].

3.4.2. Texture coarsening processes

Defect coarsening processes occurs simultaneously with defect nucleation. Texture refinement with shear indicates that the defect nucleation rate is higher than the coarsening rate. Coarsening process include: (1) defect-defect annihilation, (2)

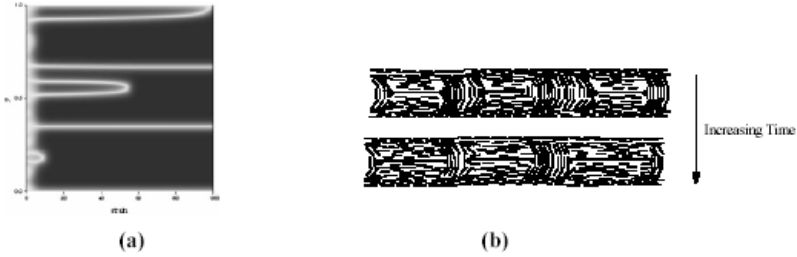


Figure 35. (a) Coarsening by defect-defect annihilation and defect-boundary annihilation; Adapted from Ref. [105] (b) Coarsening by inversion wall pinching into disclination lines; Adapted from Ref. [106].

defect-boundary annihilation, and (3) wall pinching and retraction. The first two mechanisms under shear flow are illustrated in Figure 35a for the case of non-singular inversion wall defects, where the vertical axis is the thickness direction and the strain is the horizontal axis, and Figure 35b shows a schematic of defect wall pinching with subsequent relaxation. The former figure shows how two oppositely charged inversion walls collide and annihilate leaving behind a homogeneous field and also how an inversion wall defect is attracted to the boundary where it is extinguished. Figure 35b shows that when the interfacial tension of a wall defect increases beyond a critical value it will tend to pinch producing pair of oppositely charged disclination lines which then can interact with other lines [106].

As shown above defect-defect annihilation is a mechanism that describes the elimination of heterogeneous orientation by the reaction between oppositely charged defects [1]. The interaction between oppositely charged defects in the absence of flow is characterized by an elastic force Υ_e inversely proportional to their separation distance [1]:

$$\Upsilon_e \propto K \frac{M_1 M_2}{d} \quad (58)$$

where K is the Frank elastic constant, $\{M_i; i = 1, 2\}$ are the defect charges of the two defects, and d is their separation distance. The defect motion law is then

$$\Upsilon_e = \gamma_1 \mathbf{v}_d \quad (59)$$

where \mathbf{v}_d is the defect velocity and γ_1 is the rotational viscosity. In the presence of shear, a flow force Υ_s arises and the defect motion is hindered by the presence of flow-alignment:

$$\Upsilon_e + \Upsilon_s = \gamma_1 \mathbf{v}_d \quad (60)$$

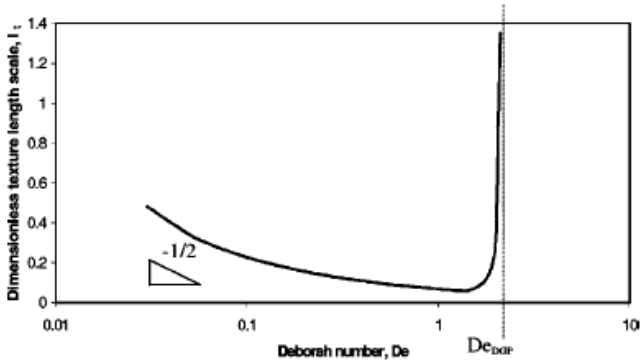


Figure 36. 1D LdG predictions of dimensionless texture length scale l_t as a function of Deborah number, showing an initial refinement of slope $-1/2$, reaching a minimum scale close to $De=1$ and diverging when De is close to 2. Adapted from Ref. [107].

The nature of Υ_s is elucidated when considering the viscous torques $(\Gamma_\theta, \Gamma_\varphi)$ acting on the director orientation $(n_x = \cos \theta \cos \varphi, n_y = \cos \theta \sin \varphi, n_z = \sin \theta)$, when subjected to a shear flow $(v_x = \dot{\gamma}z)$ [1]:

$$\Gamma_\theta = \dot{\gamma}(\alpha_3 \cos^2 \theta - \alpha_2 \cos^2 \theta) \cos \varphi; \quad \Gamma_\varphi = -\dot{\gamma} \alpha_2 \sin \theta \sin \varphi \quad (61)$$

For flow-aligning materials these two torques vanish when $(\theta = \theta_{al}, \varphi = 0)$. When a defect moves through a particular region of the bulk, the orientation changes such that $(\theta \neq \theta_{al}, \varphi \neq 0)$ and the viscous torques (eqn.(61)) resist the defect motion: $\Gamma_\theta \neq 0, \Gamma_\varphi \neq 0$. The non-vanishing viscous torques are the origin of flow force Υ_s (eqn.(60)). Hence flow-alignment can stabilize a texture by hindering coarsening through defect motion.

Defect-boundary interactions arise when the orientation at the wall is such that it generates image charges [1,53] that attract the wall to the boundary. In such case the boundary may adsorb the defect, as in the upper edge of Figure 35a. Again, close to the wall shear effects resist the defect-wall interaction.

Defect pinching is a mechanism that operates in 2D inversion walls [1,53]. When the 2D inversion walls become too thin, the gradient elastic energy increases and the wall pinches by nucleating a pair of oppositely charged $1/2$ defects. These defects then move into the wall and dissolve it [53]. The 1D simulations presented here preferentially self-select this efficient coarsening mechanism over defect-defect annihilation and defect-wall interaction.

Numerical simulation based on 1D LdG nematodynamics that take into account the three mechanisms mentioned above predict that in the presence of nucleation and

coarsening the texture length scale l_t given by the system size divided by the number of defects, follows a decreasing function of slope close to $-1/2$, reaches a minimum close to $D_e=1$ and then diverges close to $D_e \approx 2$, as shown in Figure 36, for $\square = 10^6$ [107].

According to LdG nematodynamics [107], defect nucleation is only a function of the Ericksen number, and hence changing the temperature U will only affect coarsening processes. The transition dimensionless temperature that indicates the boundary between polydomain and monodomain textures for $\square = 10^6$ is $T/T^* = 1/U \approx 0.4 - 0.18D_e^{0.2}$. The predictions indicate that as the temperature of the LC lowers the De needed to attain a monodomain increases.

4. LINEAR AND NONLINEAR VISCOELASTICITY OF CARBONACEOUS MESOPHASE BASED ON LESLIE-ERICKSEN CAPILLARY NEMATODYNAMICS

The capillary rheometry and steady Poiseuille flows of carbonaceous mesophases has been reported [108-112]. These studies show how heterogeneous shear rate creates a range of flow-induced textures, and textural transformations. Simulations on capillaries indicates that the apparent viscosity in steady Poiseuille flow can be of the shear thinning type or non-monotonic, depending on the anchoring conditions and orientation. As mentioned above transient nematic flows are characterized by backflows, viscosity reduction mechanisms, and transient re-orientation effects on velocity and offer a unique window opportunity to characterize the viscoelasticity of nematic materials. In this section we investigate flow start-up, and cessation of flow.

4.1. Governing Equations

For Poiseuille capillary flow, using cylindrical coordinate system, axisymmetric planar director field $(\mathbf{n}(\mathbf{r}, t) = (\sin\theta(\mathbf{r}, t), 0, \cos\theta(\mathbf{r}, t)))$ and purely axial velocity field $(\mathbf{v}(\mathbf{r}, t) = (0, 0, v(\mathbf{r}, t)))$ the transient dimensionless governing equations for the director tilt angle $\theta(\tilde{r}, \tilde{t})$ and the axial velocity $\tilde{v}(\tilde{r}, \tilde{t})$ are [113]:

$$\frac{\partial\theta}{\partial\tilde{t}} = \frac{(\cos^2\theta + \varepsilon \sin^2\theta)}{\tilde{\Upsilon}(\theta)} \left[\frac{\partial^2\theta}{\partial\tilde{r}^2} + \frac{1}{\tilde{r}} \frac{\partial\theta}{\partial\tilde{r}} \right] + \tag{62}$$

$$\frac{\sin 2\theta}{2\tilde{\Upsilon}(\theta)} \left[(\varepsilon - 1) \left(\frac{\partial\theta}{\partial\tilde{r}} \right)^2 - \frac{1}{\tilde{r}^2} \right] - \left[\frac{\tilde{U}(\theta)}{2} \frac{E_r}{\tilde{G}(\theta)\tilde{\Upsilon}(\theta)} \right] \tilde{r}$$

$$\frac{\partial\tilde{v}}{\partial\tilde{r}} = - \left(\frac{\tilde{r}}{2\tilde{G}(\theta)} \right) E_r + \tilde{B} \left(\theta, \frac{\partial\theta}{\partial\tilde{t}} \right) \tag{63}$$

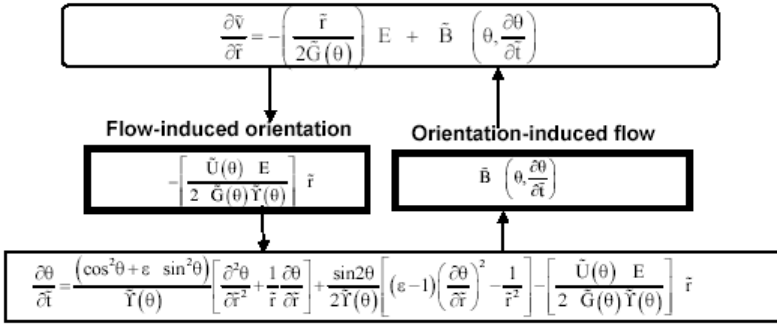


Figure 37. Nematodynamic cycle for transient capillary flows.

$$\tilde{\Upsilon}(\theta) = \tilde{\gamma}_1 - \frac{\tilde{U}^2(\theta)}{\tilde{G}(\theta)} \quad (64)$$

$$\tilde{G}(\theta) = \tilde{\alpha}_4 \sin^2 \theta \cos^2 \theta + \frac{(\tilde{\alpha}_5 - \tilde{\alpha}_2)}{2} \sin^2 \theta + \frac{(\tilde{\alpha}_3 + \tilde{\alpha}_6)}{2} \cos^2 \theta + \frac{\tilde{\alpha}_4}{2} \quad (65)$$

$$\tilde{U}(\theta) = \tilde{\alpha}_2 \sin^2 \theta - \tilde{\alpha}_3 \cos^2 \theta \quad (66)$$

$$\tilde{B} \left(\theta, \frac{\partial \theta}{\partial \tilde{t}} \right) = \left(\frac{\tilde{U}(\theta)}{\tilde{G}(\theta)} \right) \frac{\partial \theta}{\partial \tilde{t}} \quad (67)$$

where the $\tilde{\alpha}_i$, $i=1-6$, are the dimensionless Leslie viscosities ($\tilde{\alpha}_i = \alpha_i / \langle \eta \rangle$), $\langle \eta \rangle$ is the average Miesowicz' viscosity (discussed in detail in section 2.2), $\varepsilon = K_{33} / K_{11}$ is the ratio of the bend and the splay Frank elastic constants, $E_r = R^3 (-dp/dz) / K_{11}$ is the ratio of viscous flow effects to long-range elasticity effects known as the Ericksen number, $\tilde{r} = r/R$ is the dimensionless radius, R is the capillary radius, $\tilde{t} = K_{11} t / (R^2 \langle \eta \rangle)$ is the dimensionless time, $\tilde{v} = \langle \eta \rangle R v / K_{11}$ is the scaled axial velocity, $-dp/dz$ is the given pressure drop in the capillary per unit length, \tilde{B} is the dimensionless backflow, $\tilde{\Upsilon}(\theta)$ is the dimensionless re-orientation viscosity and $U^2(\theta)/G(\theta)$ is the backflow viscosity function (see eqn.(64)). The boundary conditions for the director orientation angle are: $(\theta(0, \tilde{t}) = \theta(1, \tilde{t}) = 0)$, and represent edge-on anchoring. For the axial velocity we use the no slip condition at the bounding surface: $\tilde{v}(1, \tilde{t}) = 0$.

According to the nematodynamics cycle, for transient capillary flows we find, as shown in Figure 37, that the viscoelastic material function for flow-induced orientation is $\tilde{U}(\theta)/\tilde{G}(\theta)\tilde{\Upsilon}(\theta)$ and for orientation-induced flow is $\tilde{U}(\theta)/\tilde{G}(\theta)$.

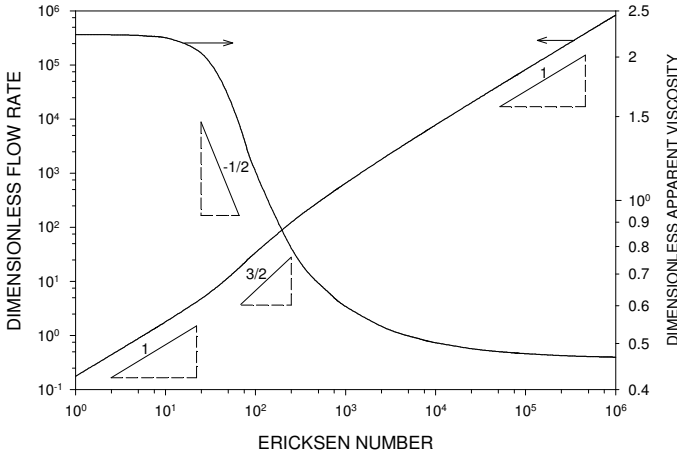


Figure 38. Apparent viscosity and flow rate as a function of the Ericksen number E_r . The slopes indicate the power-law exponent. Adapted from Ref. [112].

In steady Poiseuille flow the main non-Newtonian rheological features are captured by the dimensionless flow rate (\tilde{Q}), and the dimensionless apparent viscosity ($\tilde{\eta}_{app}$) [112]:

$$\tilde{Q} = 2\pi \int_0^1 \tilde{v}(\tilde{r}) \tilde{r} d\tilde{r}, \quad \tilde{\eta}_{app} = \frac{\pi E_r}{8\tilde{Q}} \quad (68)$$

Figure 38 shows the dimensionless flow rate, and the apparent viscosity as a function of E_r , for the boundary conditions ($\theta(0) = \theta(1) = 0$). According to the Ericksen-Leslie model, the apparent viscosity follows the classical three regions of shear thinning materials. The two viscosity plateaus correspond to [112]:

$$\lim_{E_r \rightarrow 0} \tilde{\eta}_{app} = \tilde{\eta}_l, \quad \lim_{E_r \rightarrow \infty} \tilde{\eta}_{app} = \tilde{\eta}_{al} = \tilde{\eta}_l + \frac{1}{2}(\tilde{\eta}_2 - \tilde{\eta}_l) \left(1 - \frac{1}{\lambda}\right) \quad (69)$$

where $\tilde{\eta}_{al}$ is the alignment viscosity. In the power law region we find: $\tilde{\eta}_{al} \propto E_r^{-1/2}$. The Ericksen-Leslie model predicts an exponent of $-1/2$. The three regions in the dimensionless flow rate correspond to the three regions of the viscosity. At low and high E_r , the flow rate is linear in E_r , and in the power-law region, the flow rate scales with $E_r^{3/2}$. Given this classical shear thinning behavior, in this paper we wish to establish whether the transient responses are also classical.

In both linear and non-linear regimes the calculations are performed using a set of characteristic DNLCs viscoelastic material parameters listed in Table I of [114],

which correspond to the six scaled Leslie coefficients calculated from non-equilibrium molecular dynamics simulations and the Frank elastic constants measured to hexakis(dodecanoyloxy)truxene [114].

TABLE I. Material Parameters [114].

| Dimensionless Leslie viscosities coefficients ($\tilde{\alpha}_i = \alpha_i / \langle \eta \rangle$)* | |
|---|--------|
| $\tilde{\alpha}_1$ | 0.000 |
| $\tilde{\alpha}_2$ | 0.341 |
| $\tilde{\alpha}_3$ | 1.765 |
| $\tilde{\alpha}_4$ | 1.293 |
| $\tilde{\alpha}_5$ | -0.705 |
| $\tilde{\alpha}_6$ | 1.402 |
| Frank elastic constants (10^{-12} N) | |
| K_{11} | 3.50 |
| K_{33} | 5.75 |

*The average Miesowicz's viscosity $\langle \eta \rangle$ is defined as $(\eta_1 + \eta_2 + \eta_3)/3$

The essential features of the solutions and the main conclusions of this paper will remain unaffected if the reactive parameter (λ) is less than minus one and if the Miesowicz' inequalities, discussed in section 2.2.2, hold [66].

4.2. Material Functions

The true viscosity for this capillary flow is:

$$\tilde{\eta}(\tilde{t}) = \frac{\tilde{\sigma}_{rz} \Big|_{\tilde{r}=1}}{\frac{\partial \tilde{v}_z}{\partial \tilde{r}} \Big|_{\tilde{r}=1}} \quad (70)$$

where the shear stress $\tilde{\sigma}_{rz}$ is:

$$\tilde{\sigma}_{rz} = \tilde{G}(\theta) \frac{\partial \tilde{v}_z}{\partial \tilde{r}} - \tilde{U}(\theta) \frac{\partial \theta}{\partial \tilde{t}} \quad (71)$$

Using Eq.(10,62,63), Eq.(70) becomes;

$$\tilde{\eta}(\tilde{t}) = \tilde{G}(\theta = 0) = \tilde{\eta}_i \quad (72)$$

The functions we analyze are: (a) flow rate, (b) recoil volume (for cessation of flow), (c) final recoil envelope (for cessation of flow), (d) Frank elastic energy, as follows:

(a) The transient dimensionless flow rate $\tilde{Q}(\tilde{t})$ is calculated by Eq.(68). To discuss the results it is useful to introduce the following normalized transient flow rates:

$$\tilde{Q}_s(\tilde{t}) = \frac{\tilde{Q}(\tilde{t}) - \tilde{Q}(0)}{\tilde{Q}(\infty) - \tilde{Q}(0)} \quad (73)$$

(b) Using Eq.(12) and the axisymmetric planar director field expression the transient total dimensionless elastic energy $\tilde{F}(E_r, \tilde{t})$ simplifies to :

$$\tilde{F}(E_r, \tilde{t}) = \int_0^1 \left\{ \left(\frac{\partial \theta}{\partial \tilde{r}} \right)^2 \left[\cos^2 \theta(\tilde{r}) + \varepsilon \sin^2 \theta(\tilde{r}) \right] + \frac{\partial \theta}{\partial \tilde{r}} \frac{\sin 2\theta(\tilde{r})}{\tilde{r}} + \frac{\sin^2 \theta(\tilde{r})}{\tilde{r}^2} \right\} \tilde{r} d\tilde{r} \quad (74)$$

(c) To characterize cessation of flow we use the recoil volume. It is assumed that at time t=0 the previously imposed pressure drop, corresponding to an Ericksen number E_r , is set equal to zero. A backflow is then generated, whose magnitude depends on previously imposed E_r . The dimensionless recoil volume $\tilde{V}_r(E_r)$ is calculated using the expression:

$$\tilde{V}_r(E_r) = - \int_0^\infty \tilde{Q}(\tilde{t}) d\tilde{t} \quad (75)$$

(d) The axisymmetric surface of the recoil volume maybe assessed experimentally using markers or other experimental methods. The final dimensionless recoil envelope is calculated using the expression:

$$\tilde{z}_r(\tilde{r}) = \int_0^\infty \tilde{v}(\tilde{t}, \tilde{r}) d\tilde{t} \quad (76)$$

where $\tilde{z}_r(\tilde{r})$ is the axial coordinate of the recoil surface at a radial distance. Rotating the recoil envelope by 2π radians around the pipe axis defines the surface of the recoil volume.

4.3. Linear viscoelasticity

The linear regime of CMs under transient capillary Poiseuille flow arises whenever E_r is sufficiently small. By comparing numerical and analytical results we found that significant deviations from the linearized equations occur for $E_r > 20$; however, for $E_r < 20$ the numerical and analytical results are practically identical. To solve analytically the linearized equations we must assume that $\varepsilon = 1$, or $K_{11} = K_{33} = K$. In this regime the amplitude of the re-orientation is small and the response is characterized by the “bare” material properties, such as the appropriate Miesowicz viscosity, re-orientation viscosity, and orientation diffusivity.

Considering $\varepsilon = 1$, and linearizing the director components around the axial direction (i.e., $\sin\theta \cong \theta$, and $\cos\theta \cong 1$) the governing equations (Eqs. (62) and (63)) simplify to:

$$\frac{\partial \theta}{\partial \tilde{t}} = \frac{1}{\tilde{\eta}_{\text{splay}}} \left\{ \left[\frac{\partial}{\partial \tilde{r}} \left(\frac{1}{\tilde{r}} \frac{\partial}{\partial \tilde{r}} (\tilde{r} \theta) \right) \right] + \frac{\tilde{\alpha}_3}{2\tilde{\eta}_l} E_r^* \tilde{r} \right\} \quad (77)$$

$$\frac{\partial \tilde{v}}{\partial \tilde{r}} = -\frac{1}{2\tilde{\eta}_l} \left(E_r^* \tilde{r} + 2\tilde{\alpha}_3 \frac{\partial \theta}{\partial \tilde{t}} \right) \quad (78)$$

where the Ericksen number $E^*(\tilde{t}-\tilde{t}_c)$ for each flow is given by

$$(i) \text{ Start-up flow: } E_r^* = E_r \left(H(\tilde{t}-\tilde{t}_c) \right)$$

$$(ii) \text{ Cessation of flow: } E_r^* = E_r \left(1-H(\tilde{t}-\tilde{t}_c) \right)$$

and where H is the Heaviside step function and t_c is the switch time. This semi-coupled set of equations can be solved by separation of variables method. Note that the velocity partial time derivative is missing in Eq.(78), and hence the velocity time dependence is set by the director dynamics. Since when E_r is small, elasticity dominates over flow, and hence the relevant time scale is τ_0 . Thus all transient results are in terms of the previously defined dimensionless time \tilde{t} . The dimensionless backflow and the re-orientation viscosity in the linear regime for the adopted boundary conditions are given by:

$$\tilde{B} = -\frac{\tilde{\alpha}_3}{\tilde{\eta}_l} \frac{\partial \theta}{\partial \tilde{t}}, \quad \tilde{Y}(\theta) = \tilde{\eta}_{\text{splay}} \quad (79)$$

4.3.1. Start-up flow

The orientation and velocity fields upon flow start-up are:

$$\theta^+(\tilde{r}, \tilde{t}) = -\frac{\tilde{\alpha}_3}{\tilde{\eta}_l} \frac{E_r}{4} \sum_{n=1}^{\infty} J_1(\beta_n \tilde{r}) \frac{J_3(\beta_n)}{\beta_n^2 J_2(\beta_n)^2} e^{\frac{-\beta_n^2}{4\tilde{\eta}_{\text{splay}}} \tilde{t}} + \frac{\tilde{\alpha}_3}{\tilde{\eta}_l} \frac{E_r}{16} (1-\tilde{r}^2) \tilde{r} \quad (80)$$

$$\tilde{v}^+(\tilde{r}, \tilde{t}) = \frac{E_r}{4\tilde{\eta}_l} (1-\tilde{r}^2) + \frac{E_r}{16\tilde{\eta}_{\text{splay}}} \left(\frac{\tilde{\alpha}_3}{\tilde{\eta}_l} \right)^2 \sum_{n=1}^{\infty} \frac{J_3(\beta_n)}{\beta_n^2 J_2(\beta_n)^2} (J_0(\beta_n \tilde{r}) - J_0(\beta_n)) e^{\frac{-\beta_n^2}{4\tilde{\eta}_{\text{splay}}} \tilde{t}} \quad (81)$$

$J_\nu(x)$ is the Bessel function of the first kind and order ν , and β_n are the roots of the Bessel function of the first kind and first order. The orientation and velocity fields are linear in E_r . The static spatial dependence is cubic for orientation and quadratic for velocity. The amplitude of both fields involve three distinct viscosities: the backflow viscosity $\tilde{\alpha}_3^2/\tilde{\eta}_l$, the splay re-orientation viscosity η_{splay} , and Miesowicz'

viscosity η_1 . The evolution is governed by the splay viscosity, and the dimensional relaxation times τ_n are:

$$\tau_n = \frac{4}{\beta_n^2} \left(\frac{a^2 \eta_{\text{splay}}}{K} \right), n = 1, 2, 3, \dots \quad (82)$$

Equations (80-81) shows that the orientation evolves to a cubic profile without overshoot, and the velocity evolves to the parabolic profile by relaxation of an initial overshoot.

The dimensionless flow rate $\tilde{Q}^+(\tilde{t})$, obtained using Eq.(68,73, 81), is given by:

$$\tilde{Q}^+(\tilde{t}) = \frac{\pi E_r}{8\tilde{\eta}_1} - \frac{\pi E_r}{16\tilde{\eta}_{\text{splay}}} \left(\frac{\tilde{\alpha}_3}{\tilde{\eta}_1} \right)^2 \sum_{n=1}^{\infty} \frac{J_3(\beta_n) J_0(\beta_n)}{J_2(\beta_n)^2 \beta_n} e^{-\frac{\beta_n^2}{4\tilde{\eta}_{\text{splay}}} \tilde{t}} \quad (83)$$

The relaxation of $\tilde{Q}^+(\tilde{t})$ is characterized by the relaxation times defined in Eq.(82). At steady state the dimensionless flow rate is $\tilde{Q}^+(\infty) = \pi E / 8\tilde{\eta}_1$, which is a linear function of E_r .

4.3.2. Cessation of flow

The orientation and velocity upon cessation of steady flow are:

$$\theta^-(\tilde{r}, \tilde{t}) = \frac{\tilde{\alpha}_3}{\tilde{\eta}_1} \frac{E_r}{4} \sum_{n=1}^{\infty} J_1(\beta_n \tilde{r}) \frac{J_3(\beta_n)}{\beta_n^2 J_2(\beta_n)^2} e^{-\frac{\beta_n^2}{4\tilde{\eta}_{\text{splay}}} \tilde{t}} \quad (84)$$

$$\tilde{v}^-(\tilde{r}, \tilde{t}) = \frac{E_r}{16\tilde{\eta}_{\text{splay}}} \left(\frac{\tilde{\alpha}_3}{\tilde{\eta}_1} \right)^2 \sum_{n=1}^{\infty} \left(\frac{J_3(\beta_n)}{\beta_n J_2(\beta_n)^2} e^{-\frac{\beta_n^2}{4\tilde{\eta}_{\text{splay}}} \tilde{t}} \times \right. \\ \left. (J_0(\beta_n) - J_0(\beta_n \tilde{r})) \right) \quad (85)$$

The dynamics of the relaxation, as well as the amplitudes involve essentially the same relaxation times, and viscosities as in start-up.

The dimensionless recoil volume $\tilde{V}_r(E_r)$ is given by:

$$\tilde{V}_r(E) = -\frac{\pi E_r}{4} \left(\frac{\tilde{\alpha}_3}{\tilde{\eta}_1} \right)^2 \sum_{n=1}^{\infty} \frac{J_3(\beta_n) J_0(\beta_n)}{\beta_n^3 J_2(\beta_n)^2} \quad (86)$$

The recoil volume $\tilde{V}_r(E)$ is linear in E and scales with the backflow viscosity $\tilde{\alpha}_3^2 / \tilde{\eta}_1$. Recoil in sheared CMs is driven by the stored Frank elastic energy. The stored

dimensionless total energy per unit length $\tilde{F}(E_r)$ at cessation, calculated using Eqs.(74) with $\varepsilon=1$, gives:

$$\tilde{F}(E) = \frac{E_r^2}{32} \left(\frac{\tilde{\alpha}_3}{\tilde{\eta}_l} \right)^2 \sum_{n=1}^{\infty} \frac{J_3(\beta_n)^2 J_0(\beta_n)^2}{\beta_n^2 J_2(\beta_n)^4} \quad (87)$$

The stored energy at cessation is quadratic in E , while the recoil volume is linear in E . This is due to the fact that the energy is quadratic in director gradients but the velocity is proportional to the director velocity. The stored elastic energy drives the recoil, and that the crossover is at $E_r \sim 7$. Computational results from the full equations show that the linear results are accurate up to $E_r \sim 50$. Since displacements due to recoil may be detected by particle displacements, we can use the final position of marked particles to characterize the envelope of the recoil volume. The recoil envelope is an axisymmetric surface defined in Eq.(76) and given by:

$$\tilde{z}_r(\tilde{r}) = \frac{E_r}{4} \left(\frac{\tilde{\alpha}_3}{\tilde{\eta}_l} \right)^2 \sum_{n=1}^{\infty} \frac{J_3(\beta_n)}{\beta_n^3 J_2(\beta_n)^2} (J_0(\beta_n) - J_0(\beta_n \tilde{r})) \quad (88)$$

For small E the recoil envelope is almost Gaussian, with an amplitude that scales with E . Recoil measurements provide information on the backflow viscosity and the previously applied Ericksen number; if the material properties are known then recoil can be used as a manometer, as shown in [115].

4.4. Non-linear viscoelasticity

In this regime E_r is relatively large, and flow dominates over elasticity. Thus the proper time scale that describes the transient process is the flow time scale τ_f :

$$\tau_f = \frac{1}{\dot{\gamma}} = \frac{\langle \eta \rangle}{R(-dp/dz)} \quad (89)$$

where $\dot{\gamma}$ is the effective strain rate. Thus all transient results in the non-linear regime are shown as a function of strain $\gamma = \dot{\gamma}t = \tilde{t}E_r$. In addition the amplitude of the re-orientations are large and the response creates strong backflow effects and significant viscosity reduction; the backflow (\tilde{B}) and the backflow viscosity ($U^2(\theta)/G(\theta)$) are now complex non-linear functions of the director field (see Eqs.(64) to (67)).

4.4.1. *Start-up flow*

Figure 39 shows the transient normalized flow-rate $\tilde{Q}^+(\tilde{t})$ as a function of the strain (γ), $\varepsilon=1.64$, and $E_r = 500, 2500, 5000$, and 20000 . Increasing E_r increases the amplitude of the overshoot. Steady states are reached in five strain units. Comparing with the linear response, the main difference is the presence of an

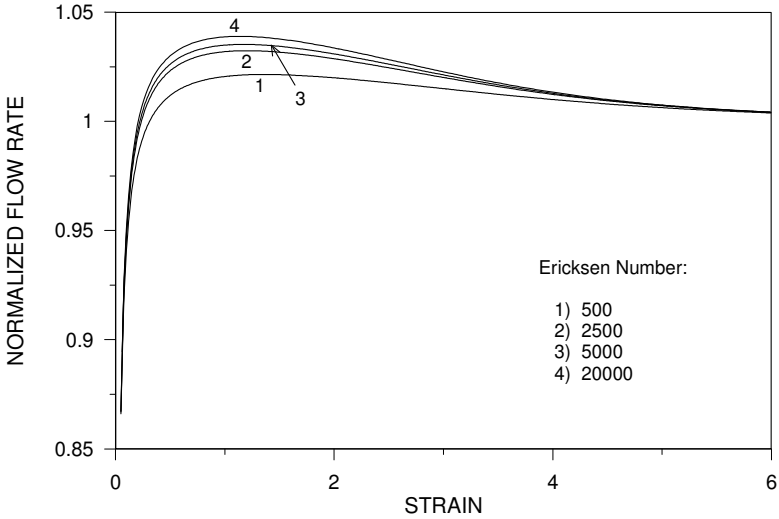


Figure 39. Normalized flow-rate (\tilde{Q}_s^+) as a function of the strain ($\gamma = \bar{\tau} E_r$) in start up flow, for Ericksen numbers (E) : 500, 2500, 5000 and 20000 and elastic factor (ϵ) :1.64. Adapted from Ref. [112].

overshoot close to $\gamma=1$. The overshoot occurs when the average director angle is close to $\pi/4$. This is analogous to the stress overshoot in simple shear.

4.4.2. Cessation of flow

Figure 40a shows the dimensionless elastic energy per unit length $\tilde{F}(E_r)$ and the dimensionless recoil volume $\tilde{V}_r(E_r)$ as a function of Ericksen Number E_r . The selected range of Ericksen numbers, $0.1 < E_r < 105$, includes linear and non-linear regimes. The figure shows that power law exponents in the linear and non-linear regimes are as follows:

- (i) linear regime : $E_r < 50, \tilde{F} \propto E_r^2, \tilde{V}_r \propto E_r^2$
- (ii) non-linear regime : $E_r > 100, \tilde{F} \propto E_r^{1/2}, \tilde{V}_r \propto E_r^0$

The power law exponents for the linear regime were discussed above. The origin of the power law exponents in the non-linear regime is found by using the following orientation boundary layer thickness δ and the characteristic axial velocity v :

$$\delta = \frac{Rc}{2\sqrt{E_r}} \left(\frac{\gamma_2}{\alpha_2} \right)^{1/4} \quad v \approx \frac{KH}{\delta^2 \eta} \quad (90)$$

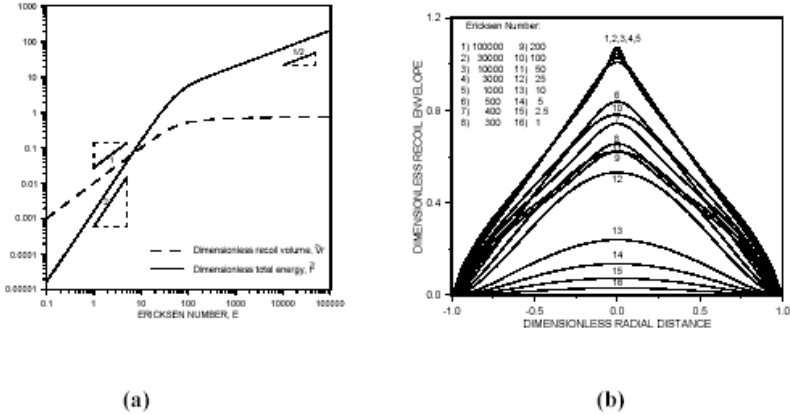


Figure 40. (a) Numerical results of the dimensionless elastic energy (\tilde{F}) and dimensionless recoil volume (\tilde{V}_r) as a function of Ericksen Number (E_r), after cessation of flow. (b) Dimensionless recoil surface (\tilde{z}_r) as a function of dimensionless radial distance (\tilde{r}) and Ericksen Number (E_r) after cessation of flow. Adapted from Ref. [112].

in the force and torque LE equations.; here H is the pipe radius and c is a material constant [112]. Figure 40b shows the dimensionless recoil envelope ($\tilde{z}_r(\tilde{r})$) as a function of the Ericksen number (E_r). The figure shows that as E_r increases in the linear regime the perimeter of the envelope increases but it maintains an almost Gaussian shape. The intermediate regime, or transition between linear and non-linear regimes, occurs around $E=50$, shows strong hysteresis and the maximum of $\tilde{z}_r(\tilde{r})$ decreases with increasing E . The non-linear regime is characterized by an almost perfect conic recoil volume. The recoil envelope can be used to assess flow strength as well as the orientation time scale τ_o .

In partial summary the LE capillary nematodynamics provides the following information: (a) Linear viscoelasticity: transient flow rates for cessation of flow, flow reversal, and flow start-up, provide a way to extract the re-orientation viscosity $\tilde{\eta}_{\text{splay}}$, the backflow viscosity $\tilde{\alpha}_3^2/\tilde{\eta}_1$, the splay re-orientation viscosity η_{splay} , the Miesowicz' viscosity η_1 , from experimental data. (b) Nonlinear viscoelasticity: the flow-rates and recoil volume signals contain information on viscoelastic materials properties and provide a clear indication of the transition between linear and non-linear regimes. Cessation of flow provides a way to measure the previously imposed flow-rate, and acts as a manometer. The sensitivity of the recoil volume to the imposed pressure drop also offers a way to detect the onset of structural changes, since its shape changes from a paraboloid at low pressure drops to a cone at higher pressure drops.

5. LANDAU-DE GENNES SHEAR NEMATODYNAMICS

5.1. Monodomain Shear Rheology of Carbonaceous Mesophases

The simulations presented in this section were performed adopting the nematodynamic cycle shown in Figure 41. The simulations use simple shear Newtonian hydrodynamics and the quadropolar order parameter dynamics is introduced in the total stress tensor (eqn.37) to compute the rheological material functions. In this formulation, viscoelastic anisotropy plays the major role. The experimental data used to validate the simulation is from Cato and Edie [116].

For $De < 1$, the monodomain rheology of carbonaceous mesophases (CMs) predicted by this model coincides with the LE ones [117]. For $De > 1$ changes in the scalar order parameter introduce another shear thinning mechanism, modifies the flow alignment angle, and all other material functions that depend on S [117]. Using a fix set of material parameters that are appropriate to CMs, the shear rheology was compared [117] with experimental data [116] that has the following distinguishing features: (I) For steady state shear viscosity for low shear rates the data shows the following five features: (1) The shape of the curve presents shear thinning followed by a plateau;(2) The shear viscosity increases with temperature;(3) The slope of the viscosity function in the shear thinning region is in the 0.4-0.5 range;(4) The location of the transition region shifts to higher shear rates as the temperature increases;(5) The viscosity curve displays a kink at the transition between shear thinning-to-plateau regions.(II) For steady state first normal stress difference the data shows these four features: (6) The measured first normal stress difference is negative at low shear rates.(7) At higher shear rates the first normal stress difference becomes positive.(8) At high shear rates the first normal stress difference is proportional with the shear rate.(9) The shear rate region over which the first normal stress difference transitions from negative to positive corresponds to the same region in which the shear viscosity kink is observed. (III) For steady state shear viscosity at high shear rates: (10) At high shear rates, the shear thinning behavior is due to viscous heating. (IV) For evolution during shear start-up: (11) After the initiation of shear flow the stress response shows a

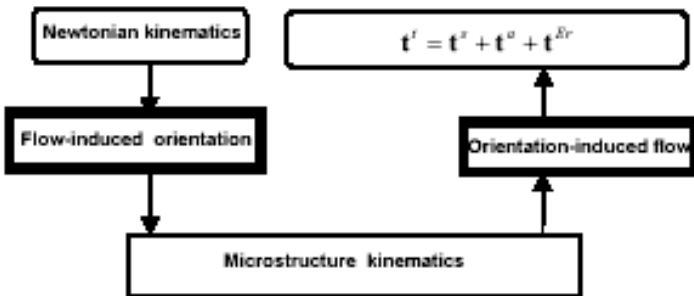


Figure 41. Simplified LdG nematodynamic cycle for monodomains.

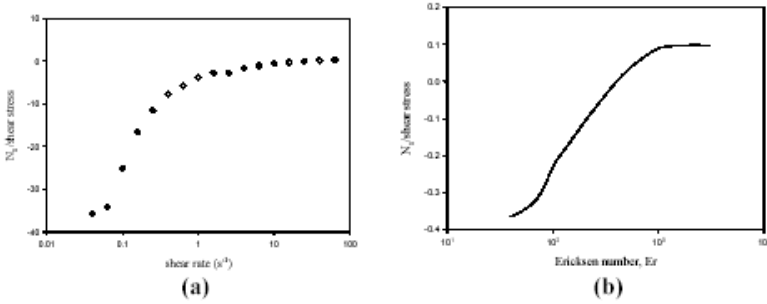


Figure 42. (a) Experimental First normal stress difference/shear stress ratio as function of shear rate. (b) Corresponding predicted signal based on the LdG nematodynamics with $1/U=0.25$, $\beta=-1.3$, $R=10^4$. Adapted from Ref. [117].

peak that relaxes toward the steady state shear stress. (12) Oscillations in the shear stress are not presented. (V) Cessation of flow: (13) After cessation of shear flow the stress response drops to zero over a time period of about 10-20 seconds.

The monodomain simulations with given constant shear rate hydrodynamics were able to qualitatively reproduce almost all the data set discussed above [116], with the exception of the kink in the viscosity, the absence of a plateau in the viscosity at low shear rates, and the temperature influence on N_1 . A summary of the validation results is shown in Table II.

For example Figure 42 shows the measured and predicted first normal stress difference/shear stress ratio as a function of shear rate. This ratio is indicative of the viscoelasticity of the material. The negative value at low shear rates is due to the fact that $N_1 < 0$. For these mesophases the origin of negative N_1 is given by equations (28-30) [117].

The growth, shape, and saturation of the first normal stress difference/shear stress ratio are well reproduced by the simplified nematodynamics. The saturation of the signal at a value of 0.11 is an indication of flow-alignment given by:

$$\left. \frac{N}{t_{xy}} \right|_{\text{flow-alignment}} = \frac{\frac{\sqrt{\lambda^2 - 1}}{2\lambda} \left(\gamma_2 - \frac{\alpha_1}{\lambda} \right)}{\frac{1}{2} (\eta_1 + \eta_2 - \gamma_1) + \frac{\alpha_1}{2} \left(\frac{\lambda^2 - 1}{\lambda^2} \right)} \quad (91)$$

Table II

Summary of agreements and disagreements between simulations from [117] and experiments from [116].

| | Experimental results in agreement with simulations | Experimental results in disagreement with simulations |
|---|--|--|
| Steady state shear viscosity for low shear rates (fig. 4,5,6 in [116] and fig. 6, 9 in [117]) | (i) shear thinning followed by a plateau (ii) shear viscosity increases as the temperature decreases (iii) the slope is 0.4-0.5 (iv) the location of the transition region shifts to higher shear rates when the temperature increases. | (i) presence of the kink (ii) absence of the plateau at very low shear rates |
| Steady state first normal stress difference (fig. 8 in [116] and fig. 8 in [117]) | (i) negative at low shear rates (ii) sign change (iii) Proportional with the shear rate for higher shear rates | (i) absence of evidence of the temperature influence |
| Steady state shear viscosity at high shear rates (fig. 10,11 in [116] and fig. 9 in [117]) | (i) at high shear rates – shear thinning | (i) decrease due to the viscous heating (simulations- decrease due to the molecular processes) |
| Shear start-up (fig. 12 in [116] and fig. 10 in [117]) | (i) no oscillations (ii) single overshoot | |
| Cessation of flow (fig. 13 in [116] and fig 11 in [117]) | (i) shear stress drops to zero in 5-10 strain units | |

5.2. Shear Rheology of Textured Carbonaceous Mesophases

Using the Carreau-Yasuda LC model (eqn.(47)) in conjunction with the texture refinement equation (57) we can estimate how the viscosity increases with increasing texture length scale l_t :

$$\eta_s = \frac{\eta - \eta_{al}}{\eta_0 - \eta_{al}} = c l_t^{2(1-n)} \left[(c l_t)^{2a} + \left(\tau H^2 + (c l_t)^2 \tau E_{r_{ADL}} \right)^a \right]^{\frac{n-1}{a}} \quad (92)$$

This result indicates that at a given shear rate, the stress growth during shear step-up should be sensitive to coarsening events. In fact the LdG model predicts that under given and constant shear rate, defect annihilation leads to stress increases. Figure 43 shows typical shear stress start-up LdG predictions adapted to CMs for $De=0.1$, $\square = 10^6$ [105]. The figure shows that when defects annihilates the texture coarsens and the shear stress grows.

5.3. Carbon fiber textures

As indicated in the introduction, melt spinning of CMs gives rise to a variety of textures. A commonly observed phenomena is that high temperatures lead to planar radial (PR) textures with a line defect at the centerline, while lower temperatures lead to a planar polar line defect (PPLD) texture, as indicated in Figure 44. Here we wish to demonstrate the effect of temperature on texture selection, specifically the PR and PPLD textures. Simple stability analysis based on the LE nematodynamics indicates that under uniaxial extensional flow the director aligns along the compression plane. Hence during fiber spinning we expect the orientation textures to be planar and the macroscopic texture selection process to be dictated by temperature (U), material properties (L_1, L_2), and fiber size (H). Figure 44 shows the LdG nematostatic texture predictions in a circular geometry for $De=0$, in terms of dimensionless temperature

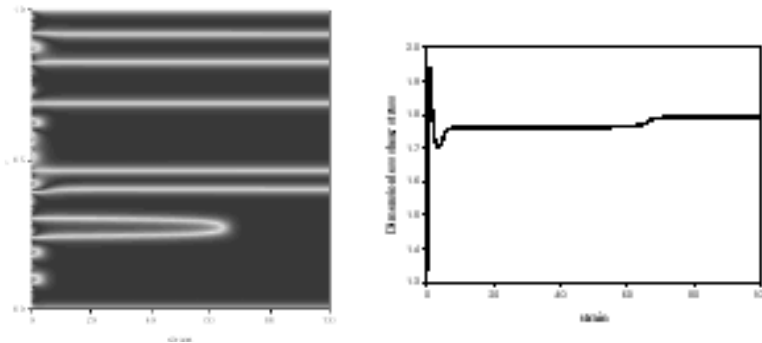


Figure 43. Computed texture (left) and corresponding shear stress (right) as a function of strain upon simple shear start-up flow. Defect annihilation leads to increased stress. Adapted from Ref. [105].

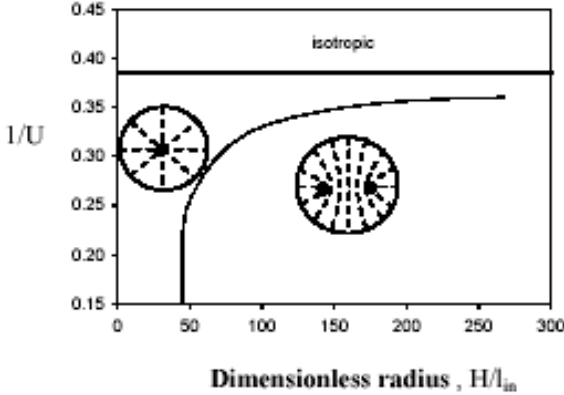


Figure 44. Texture phase diagram for $De=0$. The curve is the texture transition line. Adapted from Ref. [118].

($1/U$) and dimensionless geometry (H) [118]. The horizontal line indicates the isotropic-nematic transition. The curved line indicates the texture transition between planar polar line defect (PPLD) and the planar radial (PR) texture. The predictions of the texture transition line can be fitted to a power law of the form:

$$\frac{T}{T^*} = \frac{3}{8} - \left(\frac{H}{\ell_i} - C \right)^n \quad (93)$$

which provides a design equation for controlling texture through thermal control during the spinning of CMs; the simulations shown in Figure 44 are well fitted with $n=0.65$ and $C=37$. The predictions indicate the presence of a chimney where fiber size play no role, and a critical fiber radius below which the process is temperature-independent. The latter process is explained by the fact that defect splitting is always driven by geometry, such that for small fiber a single $+1$ is energetically preferably than two $+1/2$ disclinations. On the other hand large fibers always prefer the PPLD texture since energy scales with the square of the defect charge. At higher temperatures orientation elasticity is not dominant and there is no significant elastic driving force for defect splitting.

5.4. Simulation of Flow-Structuring

Controlled texturing in materials is possible by using specific flow geometries and by using screens, and filters. For CMs it has been shown that flow through wire screens is an efficient tool to manipulate orientation [25]. The effect is reminiscent of packing liquid crystals with submicron fibers whose positional order follows a lattice .

Figure 45 shows a schematic design of the flow geometry and resulting texturing process [119]. The wire screens are added to the spinning apparatus used for

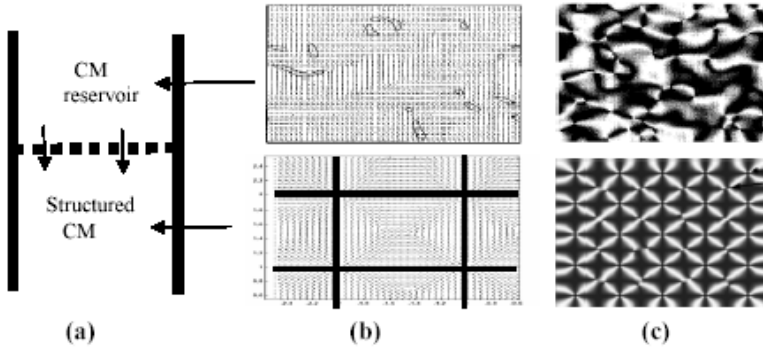


Figure 45. (a) Schematic of mesophase flow-structuring. (b) Schematic of random orientation (top) and defect lattice (bottom) computed according to LdG nematostatics ($De=0$). (c) Schematic of polarized reflection micrograph of a random texture (top) and computed reflection polarized micrograph of the defect lattice. Adapted from Ref. [119].

melt spinning of carbon fibers using CM precursors. The CM flows through a screen (dashed line in Figure 45(a)) and creates a structured mesophase consisting of a defect lattice of +1 and -1/2 defects as predicted by LdG nematostatics ($De=0$) (b); the computed reflection polarized micrograph, obtained by solving the Maxwell equations, is shown in the lower figure (c). The grid in (b) is a replica of the grid in the screen shown in (a). The upper orientation field in (b) denotes a polydomain sample that when it is forced to flow through the square grid develops a lattice structure. The upper Figure 45c is a schematic of a randomly oriented texture while the bottom one is an actual computation obtained by inputting the orientation field shown in the lower Figure 45b; each lattice in the optical response corresponds to the wire screen lattice.

A detailed view of the defect lattice shown in the bottom Figure 45b reveals that it consists of a square lattice with +1 defects at the vertices and an interpenetrating lattice consisting of a pair of -1/2 defects whose orientation is $\pm\pi/4$. Figure 46a shows the scalar order parameter S for the defect lattice and Figure 46b shows the director orientation in a unit cell; the circles are the +1 defects and the squares the -1/2 defects. The net charge in the unit cell is $M=4(+1/4)+ 2(-1/2)=0$. The experimental results show that the long memory of the CM melt render the defect lattice to be long-lived and to remain downstream in the fiber spinning process and demonstrate a way to manipulate textures.

These novel structuring results show that manipulating the flow geometry with internal surfaces and internal meshes can produce long lasting defect lattices whose symmetry replicates the internal medium.

6. SUMMARY AND OUTLOOK

In summary, a comprehensive review of flow and texture modeling of liquid crystalline materials with emphasis on carbonaceous mesophases was presented. The spatio-temporal multiscale nature of these materials was first established and used to discuss two popular models, the Leslie-Ericksen director model and the Landau-de Gennes quadropolar tensor model. The unifying themes of nematodynamics, flow-induced orientation and orientation-induced flow were used to classify rheological material functions and the impact of the nematodynamic cycle on viscoelasticity. Since liquid crystal rheology and flow-processing always occur in heterogeneous defect-filled states, a comprehensive discussion of defect physics and rheo-physics was presented. Defect classification, defect-defect interactions, defect stability, defect cores, defects under confinement, defect nucleation, and texture coarsening were discussed in relation to the two nematodynamics theories. Applications of both nematodynamic models to rheological and processing flows were presented, and the mechanisms that have impact on stress, first normal stress difference, apparent shear viscosity, recoil, and relaxation were elucidated. The role of texture refinement on rheology was discussed for simple shear start-up flow. A design equation useful to predict fiber textures was extracted from simulation data. Novel texturing methods such as flow through screens were reproduced using simple nematostatics models.

Specific insights emanating from applications of nematodynamic modeling include:

- (a) Defects and Textures: defects cores in carbonaceous mesophases can be singular or nonsingular depending on geometry and confinement; the core type is important because the associated viscoelasticity should be different

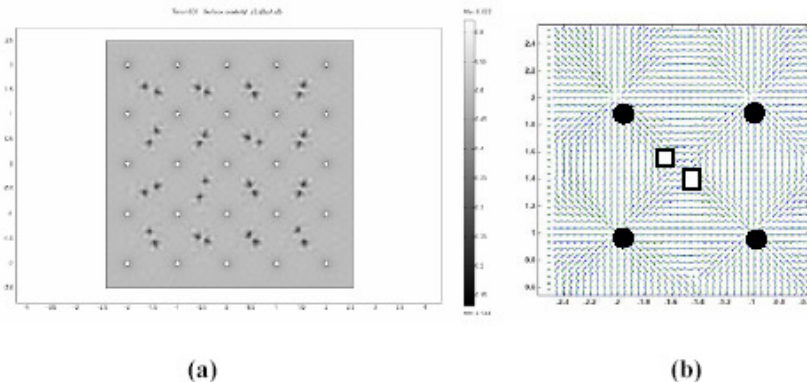


Figure 46. (a) Computed order parameter S in a defect lattice due to flow-structuring. (b) Computed orientation field in a unit cell of the defect lattice. The prediction were obtained by LdG nematostatics ($De=0$). Adapted from Ref. [119].

for micron-scale escaped orientation cores than for nanoscale disclinations. Point defects usually associated with bubbles and drops in the form of stable dipoles should nucleate during formation of CMs. Since point defects are nanoscale rings that may open up into micron scale loops, they should be considered as new sources of defects. The connection between capillary textures through disclination loop interactions and breakage provide new insights on topological transformations between textures. Flow-induced textural transformation can be rationalized in terms of defect nucleation and coarsening processes. Defect nucleations are controlled by the Ericksen number and the LdG model predicts a refinement of characteristic slope of $-1/2$. Defect coarsening is controlled by the Deborah number and the LdG model predicts a most refined texture when it is close to one. The transition between the monodomain-to-polydomain states in the temperature-Deborah number plane is a monotonic decreasing function of De , such that the further the material is from the isotropic-nematic transition the higher is the De number required to obtain monodomains.

- (b) Leslie-Ericksen Capillary Flow Nematodynamics of Carbonaceous Mesophases: these capillary flows offer a unique window on linear and non-linear viscoelasticity since flow-induced orientation and orientation-induced flow can be captured analytically and numerically. The steady viscosity can be fitted with a Carreau-Yasuda liquid crystal model, with a shear thinning region following a power law scaling with exponent equal to $-1/2$. Despite the variable shear rate, start-up and cessation of flow at small deformation rates can be solved analytically and used to determine relaxation times and anisotropic viscosities. In the nonlinear regime, numerical solutions for start-up predict the commonly observed overshoots. For cessation of flow, the stored Frank elastic energy gives rise to back-flows and conical recoil envelopes.
- (c) Landau-de Gennes Shear Flow Nematodynamics of Carbonaceous Mesophases: the monodomain predictions have been validated with experimental data. For example the ratio of shear stress to normal stress has a sigmoidal shape that saturates when the system achieves flow-alignment. Negative first normal stresses are explained by the quartic orientation non-linearity in the shear stress. Polydomain predictions capture usually observed overshoots in shear start-up and reveal that defect annihilation increases stress. Scaling prediction derived from the Carreau-Yasuda liquid crystal model in conjunction with computed polydomain texture refinement shows how the steady apparent viscosity increases with texture length scale.
- (d) Landau-de Gennes Nematostatics of Textured Carbonaceous Mesophases: the carbon fiber texture classes and thermal transitions are well predicted by the model based on elasticity and defect physics. In particular lower temperatures of micron-sized fibers naturally select textures with two $+1/2$ disclination lines to lower Frank elasticity. Simulations of nucleation of complex defect lattices by flow through screens are replicated by the model and its overall disclination content and unit lattice geometry is explained by topological charge neutrality.

Future challenges in computational rheology and processing flows are the full integration of nematodynamics with defect rheophysics. This integration is best accomplished by the direct numerical simulation (DNS) method. The challenge for DNS is to resolve the disparate length scales manifested in the large magnitude of the energy ratio \square by developing adaptable meshing methods to capture defect nucleation. Defect detection in 3D is nontrivial and it will require the development of accurate texture refinement laws. Simulations of processing flows incorporating full hydrodynamics, such as secondary flows and hydrodynamic interactions due to defect motion are almost non-existent. Interfacial nematodynamics needs to be developed to better simulate liquid crystalline foams, free surface flows, phase separation, mixing, and nano-composites. Recent [120] rheo-optical modeling based on the integration of the LE nematodynamics with the Maxwell electromagnetic equations shows good agreement with polarized optical microscopy of LCP shear flow indicating that replacing LE with LdG nematodynamics will provide a new characterization tool. Simulations of rheo-X ray and rheo-NMR have hardly been performed. Most flow-modeling has been isothermal but incorporating the thermal energy balance will prove necessary for realistic fiber melt spinning simulations. Extension of nematodynamics to cholesteric phases will be relevant to biological polymer processing and extensions to smectic phases will be useful to the understanding of biological membranes, block-copolymers and layered materials.

ACKNOWLEDGMENTS

This research was supported by the Engineering Research Centers Program of the National Science Foundation under NSF Award Number EEC-9731680, the Natural Science and Engineering Council of Canada, and the Petroleum Research Fund. This work was performed in collaboration with Dr. A.P. Singh, J. Yan, Dr. G. de Luca, Dr. B. Wincure, Dr. A-G Cheong, D. Sharma, Dr. E. Soule, M. Golmohammadi, N.M. Abukhdeir, Prof. T. Tsuji, Prof. S. Das, Prof. D. Grecov, and Prof. L. de Andrade Lima. The author is grateful to Prof. Dan Edie (Clemson University) for introducing him to the world and science of carbonaceous mesophases, to Prof. A. Ogale and Dr S. Kundu (Clemson University) for sharing their knowledge and rheological data on mesophase pitches, to Profs. C. Cox and J. Barr von Oehsen (Clemson University) for computational modeling support and advice and to the Center for Advanced Fibers and Films at Clemson University for financial support.

REFERENCES

1. de Gennes, P. G., Prost, J., *The Physics of Liquid Crystals*, 2nd edn., Oxford University Press, London (1993).
2. Donald, A. M., Windle, A. H., Hanna, S., *Liquid Crystalline Polymers*, 2nd edn., Cambridge University Press (2006).
3. Bahadur, B., *Liquid Crystals: Applications and Uses*, World Scientific, New Jersey (1992).

4. Petrov, A. G., *The Lyotropic State of Matter*, Gordon and Breach Science Publishers, Amsterdam (1999).
5. Virga, E. G., *Variational Theories for Liquid Crystals*, Chapman Hall, London (1994).
6. Peebles, L. H. Jr., *Carbon Fibers-Formation, Structure, and Properties*, CRC, Boca Raton, FL (1995).
7. Klett, J., Walls, C., Burchell, T., Ext. Abst., 24th Biennial Conference on Carbon, South Carolina, American Carbon Society (1999) p. 132.
8. Gupta, V. K., Skaife, J. J., Dubrovsky, T. B., Abbott, N. L., *Science*, 279 (1998) 2077.
9. Hwang, D. K., Rey, A. D., *J. Chem. Phys.* 125 (2006) 174902/1.
10. Rey, A. D., *Soft Matter*, 2 (2007) 1349-1368
11. Edie, D. D., Diefendorf, R. J., in *Carbon-Carbon Materials and Composites* [eds: Buckley, J. D., Edie, D. D.], Noyes Publication, Park Ridge, N. J. (1993) pp 19-37.
12. Rey, A. D., Denn, M. M., *Annu. Rev. Fluid Mech.*, 34 (2002) 233-266.
13. Larson, R., *The Structure and Rheology of Complex Fluids*, Oxford University Press, New York (1999).
14. Wang, X.-J., Zhou, Q.-F., *Liquid Crystalline Polymers*, World Scientific, Singapore (2004).
15. de Luca, G., Rey, A. D., *J. Chem. Phys.* 124 (2006) 144904/1-8.
16. Knight, D. P., Vollrath, F., *Proc. Roy. Soc. London B*, 266 (1999) 519.
17. Vollrath, F., Knight, D. P., *Nature*, 410 (2001) 541.
18. Kerkam, K., Viney, C., Kaplan, D., Lombardi, S., *Nature* 349 (1991) 349.
19. Willcox, P. J., Gido, S. P., Muller, W., Kaplan, D., *Macromolecules*, 29 (1996) 5106.
20. de Luca, G., Rey, A. D., *Phys. Rev. E*, 69 (2004) 011706
21. de Luca, G., Rey, A. D., *Eur. Phys. J. E*, 12 (2003) 291-302.
22. Neville, A. C., *Biology of Fibrous Composites*, Cambridge University Press, Cambridge (1993).
23. Zimmer, J. E., White, J. L., *Advances in Liquid Crystals*, Vol. 5 [Ed: Brown, H. G.], Academic Press, New York (1982) 157.
24. Hurt, R. H., Chen, Z. Y., *Phys. Today*, 53(3) (2000) 39.
25. Fathollahi, B., White, J. L., *J. Rheol.*, 38(5) (1994) 1591.
26. Tsuji, T., Rey, A. D., *Macromol. Theory Sim.*, 7 (1998) 623.
27. Tsuji, T., Rey, A. D., *Phys. Rev. E*, 57 (1998) 5609.

28. Tsuji, T., Rey, A. D., *J. Non-Newt. Fluid Mech.*, 73 (1997) 127.
29. Farhoudi, Y., Rey, A. D., *J. Non-Newt. Fluid Mech.*, 49 (1993) 175.
30. Farhoudi, Y., Rey, A. D., *Rheol. Acta*, 32 (1993) 207.
31. Farhoudi, Y., Rey, A. D., *J. Rheol.*, 37 (1993) 289.
32. White, J. L., Guthrie, G. L., Gardner, J. O., *Carbon* 5(5) (1967) 517.
33. Singer, L. S., Process of producing orientation in mesophase pitch by rotational motion relative to a magnetic field and carbonization of the oriented mesophase U. S. Patent 3,991,170 (1976).
34. Lewis, I. C., *Carbon* 16(6) (1978) 503.
35. Hamaguchi M., and Nishizawa, T., Fused state ¹³C NMR study on carbonaceous mesophase: orientational order and molecular motions of several aromatic compounds dissolved in carbonaceous mesophase, Carbon'92: Proc. Intern. Carbon Conf., Essen, Germany (1992) p. 45.
36. FitzGerald, J. D., Taylor, G. H., Pennock, G. M., *Microstructure of hydrogenated coal tar pitches*, Carbon'94: Proc. Intern. Carbon Conf., Granada, Spain (1994) p. 16.
37. Mochida, I., Shimizu, S., Korai, Y., Otsuke, Y., Sakai, H., Fujiyama, S., *Carbon* 26(6) (1988) 843.
38. Mochida, I., Shimizu, S., Korai, Y., Otsuke, Y., Sakai, H., Fujiyama, S., *Carbon* 28(2) (1990) 311.
39. Fujiura, R., Kojima, T., Korai, Y., Mochida, I., *Carbon'92: Carbon'92: Proc. Intern. Carbon Conf., Essen, Germany (1992)*.
40. Hutchenson, K. W., Roebbers, J. R., Thies, M. C., *Carbon* 29(2) (1991) 215.
41. Singer, L. S., High modulus high strength fibers produced from mesophase pitch U. S. Patent 4,005,183 (1977).
42. Singer, L. S., *Faraday Disc.* 79 (1985) 265.
43. Gasparoux, H., *Mol. Cryst. Liq. Cryst.*, 63 (1981) 647.
44. Brooks, J. D., Taylor, G. H., *Carbon* 3(2) (1965) 185; *Nature* 206 (1965) 697.
45. Otani S., Oya, A., *ACS Symp. Ser.*, 303 (1986) 323.
46. Edie, D. D., Dunham, M. G., *Carbon* 24(4) (1986) 477.
47. Fitzer, E., Kompalik, D., Mayer, B., *Influence of additives on pyrolysis of mesophase pitch*, Carbon'86: Proc. Intern. Carbon Conf., Baden-Baden, Germany (1986) p. 842.
48. Edie, D. D., *Pitch and Mesophase Fibers in Carbon Fibers, Filaments and Composites*, [Eds: Figueiredo J. L. et. al.], Kluwer Academic Publishers (1990).
49. Singer, L. S., *Fuel*, 60 (1981) 839.

50. McHugh, J. J., *The development of orientation in Mesophase pitch during fiber formation*, Ph. D. dissertation (1994) Clemson University, Clemson, SC, USA.
51. Nazeem F. F., Process for controlling the cross-sectional structure of mesophase pitch derived fibers U. S. Patent 4,376,747 (1983).
52. Yan, J., Rey, A. D., *Carbon*, 40(14) (2002) 2647.
53. Grecov, D., Rey, A. D., *Phys. Rev. E*, 68 (2003) 061704.
54. Grecov, D., Rey, A. D., *Mol. Cryst. Liq. Cryst.*, 391 (2003) 57.
55. Rey, A. D., *Rheol. Acta*, 40 (2001) 507-515.
56. Rey, A. D., *J. Non-Newtonian Fluid Mech.*, 96 (2001) 45.
57. Rey, A. D., *Eur. J. Phys. E*, 2 (2000) 169.
58. Rey, A. D., *Phys. Rev. E*, 61 (2000) 1540-1549.
59. Sonin, A. A., *The Surface Physics of Liquid Crystals*, Gordon and Breach Publishers, Amsterdam (1995).
60. Jerome, B., *Surface Alignment in Handbook of Liquid Crystals*, Vol. 1, [Eds: Demus, D., Goodby, J., Gray, G. W., Spiess, H. -W., Vill V.], Wiley-VCH, Weinheim (1998).
61. Yokoyama, H., *Handbook of Liquid Crystal Research*, [Eds: Collins, P. J., Patel, J. S.], Oxford University Press, New York (1997) Chap. 6, p. 179.
62. Oswald, P., Pieranski, P., *Nematic and Cholesteric Liquid Crystals*, CRC, Boca Raton, FL (2005).
63. Stewart, I. W., *The Static and Dynamic Continuum Theory of Liquid Crystals*, Taylor and Francis, London (2004).
64. Kleman, M., Lavrentovich, O. D., *Soft Matter Physics*, Springer Verlag, New York (2002).
65. Baalss, D., Hess, S., *Phys. Rev. Lett.*, 57 (1986) 86.
66. Baalss, D., Hess, S., *Z. Naturforsch. A*, 43 (1988) 662.
67. Ehrentraut, H., Hess, S., *Phys. Rev. E*, 51 (1995) 2203.
68. Sollich, H., Baalss, D., Hess, S., *Mol. Cryst. Liq. Cryst.* 168 (1989) 189.
69. Simoes, M., Domiciano, S. M., Alves, F. S., *Liq. Cryst.*, 33(7) (2006) 849.
70. Simoes, M., Domiciano, S. M., *Phys. Rev. E*, 68 (2003) 011705.
71. Lhuillier, D., Rey, A. D., *J. Non-Newt. Fluid Mech.*, 120 (2004) 85.
72. Forest, M. G., Wang, Q., Zhou, R., *J. Rheol.*, 51(1) (2007) 1.
73. Forest, M. G., Wang, Q., Zhou, R., *J. Rheol.*, 44(1) (2004) 80.
74. Srinivasarao, M., *Intern. J. Mod. Phys.*, B9 (1995) 2515.

75. Beris, A. N., Edwards, B. J., *Thermodynamics of Flowing Systems with Internal Microstructure*, Oxford University Press, New York (1994).
76. Burghardt, W. R., *Macromol. Chem. Phys.*, 199 (1998) 471.
77. Pleiner, H., Brand, H. R., in *Pattern formation in liquid crystals*. [Eds: Buka A., Kramer, L.], Springer Verlag, Vienna (1996) p. 15.
78. Marrucci, G., Greco, F., *Adv. Chem. Phys.*, LXXXVI (1993) 331.
79. Sgalari, G., Leal, G. L., Feng, J. J., *J. Non-Newt. Fluid Mech.* 102(2) (2002) 361.
80. Simoes, M., Domiciano, S. M., *Phys. Rev. E*, 68 (2003) 011705.
81. Bouligand, Y., *Defect and Textures*, in *Handbook of Liquid Crystals* [Eds: Demus, D., Goodby, J., Gray, G. W., Spiess, H.-W., Vill, V.], Wiley-VCH, Chichester (1998) 406.
82. Kleman, M., *Points, Lines and Walls in Liquid Crystals, Magnetic Systems, and Various Ordered Media*, Wiley, Chichester (1983) 322.
83. Kleman, M., *Rep. Prog. Phys.*, 52 (1989) 555.
84. Kleman, M., *Defects and Textures in Liquid Crystalline Polymers*, in *Liquid Crystallinity in Polymers*. [Ed: Ciferri, A.], VCH Publishers, New York, (1991) 365.
85. Mazenko, G. F., *Fluctuations, Order, and Defects*, John Wiley & Sons, Chichester (2002).
86. Zhou, J., Park, J. O., de Luca, G., Rey, A. D., Srinivasarao, M., *Phys. Rev. Lett.*, 97(15) (2006) 157801.
87. Gupta, G., Rey, A. D., *Phys. Rev. Lett.*, 95 (2005) 127805.
88. Zimmer, J. E., Weitz, R. L., in *Ext. Abstr.*, 16th Bien. Conf. Carbon, Am. Carbon Soc., San Diego, CA (1983) 92.
89. Yan, J., Rey, A. D., *Carbon*, 41 (2003) 105.
90. Edie, D. D., Robinson, K. E., Fleurot, O., Jones, S. P., Fain, C. C., *Carbon*, 32(6) (1994) 1045.
91. Stark, H., *Phys. Rep.*, 351 (2001) 387.
92. Kamien, R. D., *Rev. Mod. Phys.*, 74 (2002) 953.
93. de Luca, G., Rey, A. D., *J. Chem. Phys.*, 127(10) (2007) 104902.
94. de Luca, G., Rey, A. D., *J. Chem. Phys.*, 126(9) (2007) 094907.
95. Wang, L., Rey, A. D., *Theory Sim. Mater. Sci. Engng.*, 5 (1997) 67.
96. Anisimov, S. I., Dzyaloshinskii, I. E., *Sov. Phys. J. E. T. P.* 36 .
97. Wincure, B., Rey, A. D., *Nano Lett.*, 7 (2007) 1474.
98. Wincure, B., Rey, A. D., *Discrete Cont. Dynam. Syst. Ser. B*, 8(3) (2007) 623.
99. Wincure, B., Rey, A. D., *Cont. Mech. Thermodynam.*, 9 (2007) 37.

100. Wincure, B., Rey, A. D., *J. Chem. Phys.*, 124(24) (2006) 244902.
101. Chuang, I., Durrer, R., Turok, N., Yurke, B., *Science*, 251 (1991) 1336.
102. Sharma, D., Rey, A. D., *Liq. Cryst.*, 30 (2003) 377.
103. de Luca, G., Rey, A. D., Structure Evolution of Spider Silk Liquid Crystalline Precursors Material, in Management of Natural Resources, Sustainable Development and Ecological Hazards, [Eds: Brebbia, C. A., Conti, M. E., Tiezzi, E.], WIT Press IBP Global, London (2007) 381.
104. Rey, A. D., *Mol. Cryst. Liq. Cryst.*, 225 (1993) 313.
105. Grecov, D., de Andrade Lima, L. R. P., Rey, A. D., *Plast. Rubber Compos.* 35(6/7) (2006) 276.
106. Rey, A. D., *Macroscopic Modeling of Dynamical Phenomena in Liquid Crystalline Materials*, in *Advances in Transport Processes*, volume IX, [Eds: Mujumdar, A. S., Mashelkar, R. A.], Elsevier, Amsterdam (1993) Chap. 5, p. 185.
107. Grecov, D., Rey, A. D., *J. Non-Newt. Fluid Mech.*, 139 (2006) 197.
108. Cato, A. D., Edie, D. D., *Carbon*, 41 (2003) 1411.
109. McHugh, J. J., Edie, D. D., *Liq. Cryst.*, 18(2) (1995) 327.
110. de Andrade Lima, L. R. P., Rey, A. D., *J. Non-Newt. Fluid Mech.*, 110(2-3) (2003) 103.
111. de Andrade Lima, L. R. P., Rey, A. D., *Mater. Res.*, 6(2) (2003) 285.
112. de Andrade Lima, L. R. P., Rey, A. D., *J. Rheol.*, 47(5) (2003) 1261.
113. Atkin, R. J., *Arch. Rat. Mech. Anal.*, 38 (1970) 225.
114. Ho, A. S. K., Rey, A. D., *Rheol. Acta*, 30 (1991) 77.
115. Pasechnik, S. V., Torchinskaya, A. V., *Mol. Cryst. Liq. Cryst.*, 331 (1999) 341.
116. Cato, A. D., Edie, D. D., *J. Rheol.*, 49 (2005) 161.
117. Grecov, D., Rey, A. D., *J. Rheol.*, 49 (2005) 175.
118. Yan, J., Rey, A. D., *Phys. Rev. E*, 65 (2002) 031713.
119. Gupta, G., Hwang, D. K., Rey, A. D., *J. Chem. Phys.*, 122 (2005) 034902.
120. Hwang, D. K., Han, W. H., Rey, A. D., *J. Non-Newt. Fluid Mech.*, 143(1) (2007) 10.